

Thesis for the Degree of Doctor of Philosophy

Kinetics of Nanoparticle Catalysis from First Principles

Mikkel Jørgensen



CHALMERS

Department of Physics
Chalmers University of Technology
Göteborg, Sweden 2019

Kinetics of Nanoparticle Catalysis
from First Principles
Mikkel Jørgensen
ISBN 978-91-7597-872-7

© Mikkel Jørgensen, 2019

Doktorsavhandlingar vid Chalmers tekniska högskola
Ny serie nr. 4553
ISSN 0346-718X

Department of Physics
Chalmers University of Technology
SE-412 96 Göteborg
Sweden
Telephone: +46 (0)31-772 1000

Cover:
Energy and entropy sampling (CO molecule on an energy-map) enable kinetic simulations (dice), which bridge the materials gap between extended surfaces and nanoparticles.

Printed at Chalmers Digitaltryck
Göteborg, Sweden 2019

Kinetics of Nanoparticle Catalysis from First Principles

Mikkel Jørgensen
Department of Physics
Chalmers University of Technology

Abstract

Modern society depends heavily on heterogeneous catalysis, which creates strong economical and environmental incentives to improve catalyst efficiency. Heterogeneous catalysts are often realized as metal nanoparticles (NPs) supported on oxide surfaces, and catalysts are traditionally developed by trial and error approaches. However, rational catalyst design can be enabled by understanding reactions on the atomic scale. Presently, computational power has matured sufficiently to obtain atomic scale insights into reaction kinetics, directly from first-principles kinetic simulations.

This thesis develops the methodologies of first-principles kinetic simulations over NPs. Multiple factors affect modeling of reactions over NPs, such as reaction energy landscapes and entropy changes during reaction. This makes it important to investigate different methodological choices, within kinetic modeling.

Herein, Complete Potential Energy Sampling (CPES) is introduced as a method to calculate adsorbate entropy. CPES directly samples the adsorbate potential energy landscape, which allows for systematic improvements over approximate models within mean-field kinetics. CPES is tested on CO-oxidation over Pt(111), where it improves agreement with experimental references. Furthermore, CPES is applied to enable accurate description of molecular entropy in zeolites.

Reaction energy landscapes on NPs are challenging to calculate as NPs contain multiple different sites. Thus, NPs are commonly approximated using extended surfaces as model systems. In this thesis, the challenge of mapping out NP reaction energy landscapes is solved pragmatically using scaling relations. Kinetic Monte Carlo simulations are used to investigate the kinetics for CO-oxidation over Pt and selective acetylene hydrogenation over Pd/Cu single-atom alloys. It is found that kinetic couplings between the NP-sites govern the kinetics. The kinetic couplings influence how turnover frequency and selectivity depend on particle size, shape, and strain. Thus, the energetics of isolated sites and extended surface models are found to have limited value as descriptors for NP catalysis.

Keywords: Heterogeneous catalysis, Nanoparticles, Methane oxidation, CO oxidation, Acetylene hydrogenation, Kinetic modeling, Mean field approximation, Kinetic Monte Carlo, Density functional theory, Entropy

List of Publications

This thesis is based on the following appended papers:

I.

Adsorbate Entropies with Complete Potential Energy Sampling in Microkinetic Modeling

M. Jørgensen and H. Grönbeck

The Journal of Physical Chemistry C, **121** (2017), 7199-7207

II.

Monte Carlo Potential Energy Sampling for Molecular Entropy in Zeolites

M. Jørgensen, L. Chen, and H. Grönbeck

The Journal of Physical Chemistry C, **122** (2018), 20351-20357

III.

MonteCoffee: A Programmable Kinetic Monte Carlo Framework

M. Jørgensen and H. Grönbeck

The Journal of Chemical Physics, **149** (2018), 114101

IV.

First-Principles Microkinetic Modeling of Methane Oxidation over Pd(100) and Pd(111)

M. Jørgensen and H. Grönbeck

ACS Catalysis, **6** (2016), 6730-6738

V.

Connection between Macroscopic Kinetic Measurables and the Degree of Rate Control

M. Jørgensen and H. Grönbeck

Catalysis Science & Technology, **7** (2017), 4034-4040

VI.

Scaling Relations and Kinetic Monte Carlo Simulations to Bridge the Materials Gap in Heterogeneous Catalysis

M. Jørgensen and H. Grönbeck

ACS Catalysis, **7** (2017), 5054-5061

VII.

The Site-Assembly Determines Catalytic Activity of Nanoparticles

M. Jørgensen and H. Grönbeck

Angewandte Chemie International Edition, **57** (2018), 5086-5089

VIII.

Strain Affects CO Oxidation on Metallic Nanoparticles Non-Linearly

M. Jørgensen and H. Grönbeck

Topics in Catalysis (Accepted)

IX.

Influence of Atomic Site-Specific Strain on Catalytic Activity of Supported Nanoparticles

T. N. Pingel, M. Jørgensen, A. B. Yankovich,

H. Grönbeck, and E. Olsson

Nature Communications, **9** (2018), 2722

X.

Selective Acetylene Hydrogenation over Single-Atom Alloy Nanoparticles by Kinetic Monte Carlo

M. Jørgensen and H. Grönbeck

Manuscript submitted

My contributions to the publications

Paper I

I programmed the kinetic mean-field code and performed all the calculations. I wrote the first draft of the paper, which was finalized together with my coauthor.

Paper II

I programmed the Monte Carlo code and performed all static DFT calculations. I wrote the first draft of the paper, which was finalized together with my coauthors.

Paper III

I programmed the kinetic Monte Carlo modules described in the paper. I wrote the first draft of the paper, which was finalized together with my coauthor.

Paper IV

I programmed the kinetic mean-field code and performed all the calculations. I wrote the first draft of the paper, which was finalized together with my coauthor.

Paper V

I derived the equations, and performed the numerical simulations. I wrote the first draft of the paper, which was finalized together with my coauthor.

Paper VI

I programmed the kinetic Monte Carlo code and performed all the calculations. I wrote the first draft of the paper, which was finalized together with my coauthor.

Paper VII

I programmed the kinetic Monte Carlo code and performed all the calculations. I wrote the first draft of the paper, which was finalized together with my coauthor.

Paper VIII

I programmed the kinetic Monte Carlo code and performed all the calculations. I wrote the first draft of the paper, which was finalized together with my coauthor.

Paper IX

I programmed the kinetic Monte Carlo code and performed all the calculations. I wrote the first draft of the theoretical part of the paper together with H. Grönbeck. The paper was finalized by all coauthors.

Paper X

I programmed the kinetic Monte Carlo code and performed all the calculations. I wrote the first draft of the manuscript, which was finalized together with my coauthor.

Contents

1	Introduction	1
1.1	From Phenomenology Towards Microscopic Understanding	2
1.2	Thesis Objectives	4
2	Rate Constants From First-Principles	7
2.1	Density Functional Theory and Implementation	7
2.1.1	Exchange Correlation Energy Approximations	9
2.1.2	Projector-Augmented Wave Method	10
2.1.3	Periodic Systems	11
2.2	Local Minimum Structures and Energies	12
2.3	Reaction Rate Constants	12
2.4	Energy Barriers with Nudged Elastic Band Calculations	14
2.5	Adsorbate-Adsorbate Interactions	15
2.6	Modeling Entropy in Catalytic Reactions	16
2.6.1	Gas-phase Molecules	16
2.6.2	Adsorbates	17
2.6.3	Influence of Entropy in Kinetics	20
3	Methods of Kinetic Modeling	23
3.1	Chemical Master Equation	23
3.2	Mean-Field Approximation	24
3.3	Kinetic Monte Carlo	26
3.3.1	Observing Rare Events	28
3.4	Analyzing Reaction Kinetics	31
3.4.1	Reaction Mechanisms	31
3.4.2	Turnover Frequencies and Coverages	31
3.4.3	Reaction Orders and Apparent Activation Energies	31
3.4.4	Degree of Rate Control	32
3.5	Practical Formulation of Kinetic Models	33
3.6	Example: Analysis of Complete Methane Oxidation	34
4	Reactions on Nanoparticles	39
4.1	Energy Landscape Representation	39
4.2	Reaction Mechanisms	42
4.3	Effects of Particle Morphology	45
4.4	The Strain-Activity Relation	46
4.5	A Hierarchy of Effects	48
4.6	Methodological Considerations in Kinetic Modeling	49
5	Conclusion & Outlook	51
	Acknowledgments	53

Chapter 1

Introduction

"What would happen if we could arrange the atoms one by one the way we want them ... I can hardly doubt that when we have some control over the arrangement of things on a small scale we will get an enormously greater range of possible properties that substances can have and of different things we can do ... Atoms on a small scale behave like nothing on a large scale, for they satisfy the laws of quantum mechanics." Richard P. Feynman(1959)¹.

This was how Richard Feynman, nearly 60 years ago, envisioned the influence that nanotechnology will have in society. Today, his visions of manipulating matter at the atomic scale is close to reality. Systems can be designed atom by atom, which is a consequence of understanding the quantum mechanical behavior of atomic systems. Insights at the smallest scale are crucial as this enables rational design, and manipulation, of properties in nanoparticle-based technologies.

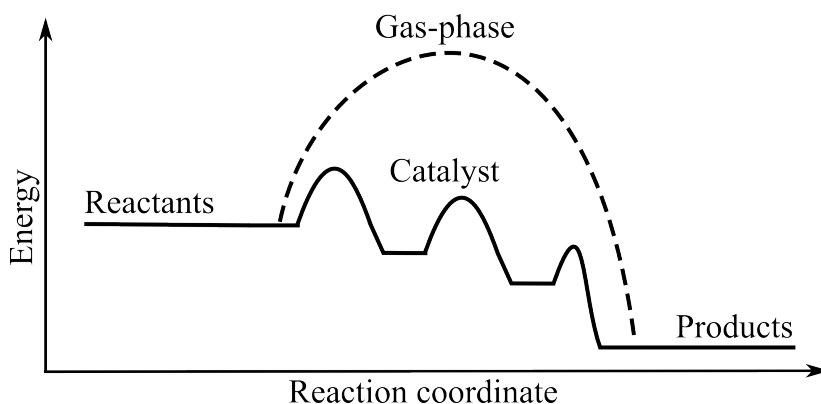


Figure 1.1: Schematic illustration of a catalytic reaction. The catalyst provides an alternative pathway with lower energy barriers for a chemical reaction.

One technology that benefits from atomistic understanding is heterogeneous catalysis. Heterogeneous catalysis is widely applied in modern society, for example in cleaning of automotive exhaust, producing synthetic fuels, and chemical manufacturing. In the chemical industry, about 90% of the production applies catalysts² (p. 11). Because of this, small improvements can have major impacts on a global scale. A catalyst is a substance that speeds up a chemical reaction without being consumed in the process. In Figure 1.1, the basic principle of a catalytic reaction is illustrated. Reactants are converted to products with lower energies as compared to the case without a catalyst. The conversion

of reactants proceeds on the surface of the catalyst, and to maximize the exposed surface area, heterogeneous catalysts are often designed as metal-nanoparticles, dispersed on porous metal-oxide supports. Catalytic cycles typically proceed in a series of steps. First, reactants adsorb onto the surface. Next, adsorbates diffuse and react, and finally the resulting products should desorb from the surface. Hence, it is important to understand chemical bonding and reactions between adsorbates on surfaces; a topic that has been investigated since the discovery of catalysis.

1.1 From Phenomenology Towards Microscopic Understanding

In 1836, J. J. Berzelius coined the term catalysis, which he explained as an invisible force that speeds up chemical reactions³. Since then, the conceptual view of heterogeneous catalysis has evolved from phenomenological laws towards insights at the microscopic scale.

Multiple conceptual models have been crucial in both disseminating and developing catalysis towards a detailed microscopic understanding. An early phenomenological model of catalysis is the Arrhenius equation, where the overall catalytic cycle is projected onto a single-reaction step. With this simplification, the total rate constant of a reaction can be quantified as^{2 (p. 36)}:

$$k = A \exp \left(\frac{-E_a}{k_B T} \right) \quad (1.1)$$

where E_a is the activation energy, A is a pre-exponential factor, and T is the temperature. As E_a appears in the exponent, small variations in E_a results in large changes in the rate. A lower activation energy allows for a higher efficiency as the temperature can be kept low. The Arrhenius equation does not describe the different partial steps that constitute a catalytic cycle: Adsorption, diffusion, reaction, and desorption. Adsorption is necessary for catalysis to proceed on the surface. In 1916, a model to describe the fraction of molecules covering a surface is formulated by I. Langmuir. The Langmuir model assumes equilibrium between the gas-phase species and adsorbates, an infinite homogeneous surface where each adsorbate can occupy only one site, and no adsorbate-adsorbate interactions. After adsorption, the reaction steps in the cycle can proceed via different mechanisms. One type is the Langmuir-Hinshelwood mechanism,^{2 (p. 56)} where two reactants meet at neighboring sites to react and desorb from the surface. Another type is the Mars-van Krevelen mechanism⁴, where the adsorbates react with a lattice-atom, which must be replaced to complete the catalytic cycle. A third possibility is the Eley-Rideal^{2 (p. 56)} mechanism that involves a reaction between an adsorbate and a gas-phase species. For these mechanisms to proceed efficiently, the adsorbates should not bind too strongly nor too weakly. This crucial realization is named the Sabatier principle, after its inventor^{2 (p. 264)}. The fact that there is an optimal binding energy of the adsorbates leads to the recognition that only a few sites might be active in a catalytic reaction, and the concept of active sites⁵. The Sabatier principle is connected to the Arrhenius equation on the atomistic scale, since E_a usually is correlated with the bond strengths of the reactants. This correlation is formulated in the Brønsted-Evans-Polanyi (BEP) principle^{2 (p. 267)}, which states that the transition state energy of a reaction is a linear function of the bond strength of the adsorbates. The Arrhenius equation describes

the entire catalytic cycle as one single reaction step, which generally does not allow for calculating A and E_a on the microscopic level. However, when transition state theory is introduced around 1935⁶, it becomes possible to calculate A for elementary reaction steps. Presently, all these concepts remain important foundations for understanding catalysis.

The development of experimental techniques has been crucial in forming a microscopic understanding of catalysis. In the early years of catalysis, experimental work involves discovering new catalysts by mixing compounds and observing reactions. However, in the early 20th century, it becomes possible to quantify the catalytic activity using mass spectrometers⁷. Furthermore, the structure of crystals can be analyzed after the invention of X-ray diffraction in the years 1914-1915 with the works of Max von Laue and Bragg⁸. Despite the available X-ray diffraction technique and quantification of catalytic rates, there is still a lack of insights into the structure of the catalyst-surface. Such insights are made possible by the invention of electron microscopes in the 1930s. The development of microelectronics and semiconductors after World War II, enables technological inventions forming the field of experimental surface science⁹. In experimental surface science, single-crystal surfaces are typically studied under ultra high vacuum conditions, using surface sensitive techniques. Surface symmetry, and thus, adsorbate structures can be measured by the invention of Low Energy Electron Diffraction (LEED). Moreover, the surface composition can be probed using electrons, or X-ray-based techniques, such as X-ray Photoelectron Spectroscopy (XPS) and Auger Electron Spectroscopy (AES). Similarly, Infrared Spectroscopy (IR) and Ultraviolet (UV) techniques are important in determining the species present on the surface. Temperature programmed desorption/reaction, and micro calorimetry enable quantification of the binding strength of reactants. Surface science generally investigates extended surfaces as model systems for nanoparticles, which is a method that allows for systematic investigations and clear results. However, it simultaneously gives rise to a, so-called, materials gap between the model systems and technical nanoparticle catalysts. Thus, efforts have been made to bridge the materials gap by performing experiments on increasingly complex stepped surfaces and well-defined nanoparticles¹⁰⁻¹³. While the early experimental techniques rely on a vacuum for probing the surface, presently it is becoming increasingly feasible and important to perform measurements in-situ. For example, it is possible to perform electron microscopy on particles during reaction with atomic resolution¹⁴, and XPS at elevated pressures¹⁵. Moreover, understanding catalysis over single nanoparticles is becoming a reality, for example using plasmonic techniques^{16;17}.

The microscopic understanding of catalysis is greatly enhanced by the formulation of quantum mechanics, forming the fields of computational chemistry and physics. Quantum chemical methods enable determination of molecular orbitals, band structures, and symmetry rules for chemical reactions, which have provided crucial microscopic insights¹⁸. The development of first-principles electronic structure calculations, especially density functional theory^{19;20}, plays an important role in studies of catalytic reactions²¹. Some of the earliest models of the catalyst surface are small clusters that locally mimic the active site²². These cluster models are fair approximations to explain chemical bonding between adsorbates and the catalyst surface²². With the growth of computational power, later surface slabs are applied to model extended surfaces²², which presently is the most common approach. Slab models enable quantitative descriptions of the adsorbate-surface

bond, yet explicit calculations on nanoparticles still pose a special challenge due to the system size and structural complexity. However, recently, studies of adsorption on idealized nanoparticle-models have been conducted using first-principles calculations^{23–32}.

Understanding trends in reaction energies is central to predict catalyst efficiency in the computational communities. This understanding is greatly enhanced after 1969, when the Newns-Anderson model of chemisorption is introduced³³. The Newns-Anderson model describes hybridization between the adsorbate valence orbitals and the metallic bands. This model later leads to the d-band model³⁴, which rationalizes trends in adsorption energies by the d-band center. This picture has many applications, for example, the d-band center can be a descriptor of adsorption energies for molecules on metal surfaces. Moreover, the d-band center is correlated with the coordination numbers of nanoparticle-sites, which suggests that the coordination number is a descriptor for the adsorption energies²¹.

Microscopic understanding of catalysis can be obtained from first principles using microkinetic models^{35;36}. Microkinetic models divide up the reaction in a series of elementary reaction steps, including adsorption, desorption, diffusion, and reaction between adsorbates. Thus, a microkinetic model can include a combination of Langmuir-Hinshelwood, Mars-van Krevelen, and Eley-Rideal mechanisms. A model that includes multiple plausible competing reactions allows for understanding the main reaction pathways and kinetic bottlenecks, which reveals the steps to target in catalyst design. Microkinetic models based on experimental measurements^{37–43} and first-principles calculations^{14;44–57} have been formulated for various catalytic reactions, primarily over extended surfaces. Nanoparticle kinetics has been modeled in some theoretical studies^{52;54;58;59}, however, in these studies the considered reaction energy landscapes were simplified or the reactions were schematic. Hence, there is a need to explore direct simulations of nanoparticle catalysis using first-principles-based reaction energy landscapes. This is presently a significant challenge in computational catalysis. The field of microkinetic modeling is growing, however, the number of formulated microkinetic models is still modest⁶⁰. Moreover, several different methods are used in first-principles kinetic modeling, which makes it timely to investigate and develop the general methodology; especially to take advantage of the advancing computational power and accuracy.

1.2 Thesis Objectives

The main theme of this thesis is to investigate and develop methodologies for first-principles microkinetic modeling of reactions on extended surfaces and nanoparticles. This is achieved using mean-field modeling and kinetic Monte Carlo simulations, combined with density functional theory calculations. Thus, methods for performing and analyzing microkinetic simulations are explored. From this, the factors that define efficient and effective nanoparticle catalysts are investigated, including: Reaction conditions, particle shape/size, the model system, entropy calculations, reaction energy landscapes, and particle strain.

The complex problem of characterizing what defines an efficient nanoparticle catalyst is typically solved from a reductionist standpoint, where the behavior of isolated-functioning sites are extrapolated to infer the total catalytic behavior. Often, a reaction mechanism

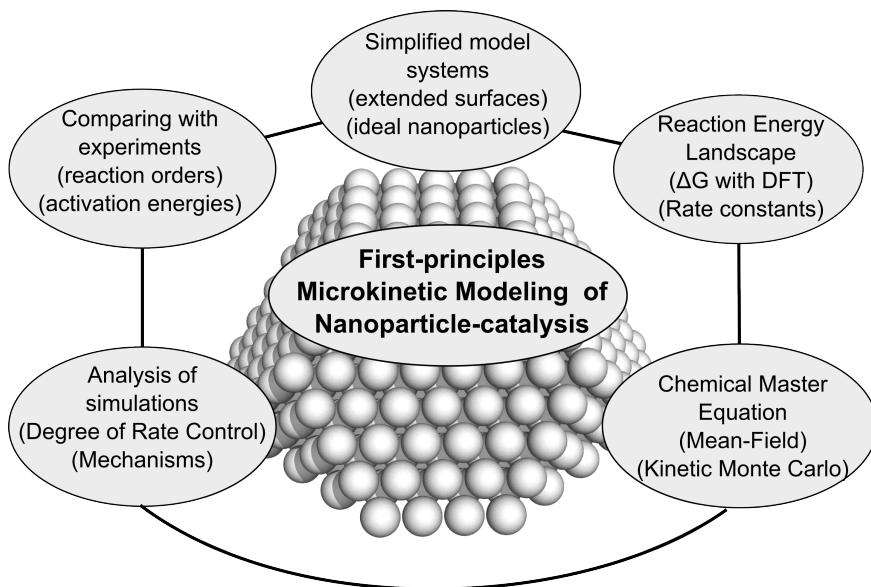


Figure 1.2: Concept map of the thesis. The map illustrates the necessary components in modeling catalysis from first principles.

and a rate-determining step are assumed to screen different materials as candidates for successful catalysts. This procedure allows for relatively affordable predictions of catalytic performance. However, chemical intuition is needed to choose a rate-determining step and dominant reaction pathway, which in the presence of multiple different sites can be deceptive, even for simple reactions. In this thesis, a systems theory approach is adopted, where sites are combined into a system that is simulated as a whole entity. Hence, the kinetic bottlenecks and dominant reaction pathways can be obtained for the system. Systemic insights aid in understanding the microscopic behavior of heterogeneous catalysis, and may ultimately improve catalyst screening.

Figure 1.2 illustrates the necessary considerations when formulating, solving, and analyzing microkinetic models. The first step is to choose a simplified model system of the catalyst. Simplification of the real catalyst is necessary as technical catalysts are complex and ill-defined. In addition, a simplified model system yields a clearer understanding of the governing mechanisms. The choice of model system can include extended surfaces as well as nanoparticles, which both are discussed in the upcoming chapters. The next ingredient in modeling is an energy landscape for the reaction, which is the set of Gibbs free energy barriers for the considered elementary reaction steps. When the Gibbs free energy barriers have been obtained, the rate constants can be calculated. Construction of the reaction energy landscape and rate constants are discussed in Chapter 2. With access to the rate constants of all elementary reactions, the kinetics can be simulated by solving the chemical master equation; either approximately in the mean-field approximation or using kinetic Monte Carlo simulations. The results of the kinetic simulations should

be analyzed to understand the governing reaction mechanisms, and to determine which elementary steps that control the rate. Here, the rate controlling steps are conveniently quantified by a degree of rate control analysis. The success of a first-principles microkinetic model depends on how well the results agree with experiments. Thus, to compare with experiments, the model can be used to predict reaction orders and apparent activation energies. Simulation of reaction kinetics and analysis of the results are treated in Chapter 3. To put the entire methodology into context, Chapter 4 discusses hydrogenation and oxidation reactions over nanoparticles, with focus on comparing nanoparticles to extended surfaces.

Chapter 2

Rate Constants From First-Principles

This chapter discusses calculations of rate constants from first-principles using density functional theory and transition state theory. The kinetics of catalytic reactions depends on the rate constants of the elementary reaction steps, which are determined by the free energy changes. The Gibbs free energy change of a reaction is the sum of enthalpy (ΔH) and entropy (ΔS) terms:

$$\Delta G = \Delta H - T\Delta S. \quad (2.1)$$

ΔH of the reaction is determined by electronic rehybridization, where bonds are broken and new bonds are formed. Similarly, ΔS is determined by the potential energy landscape. Therefore, it is essential to calculate the changes in total energy of atomic systems along the reaction path; a task that can be performed using density functional theory.

2.1 Density Functional Theory and Implementation

The total energy of a system of atoms is calculated using the stationary Schrödinger equation:

$$\hat{H} |\Psi\rangle = E |\Psi\rangle, \quad (2.2)$$

where the many-body Hamiltonian for a system of electrons and nuclei (\hat{H}) can be written:

$$\hat{H} = \hat{H}_{eZ} + \hat{H}_{ee} + \hat{H}_{ZZ}. \quad (2.3)$$

The expression (2.3) includes contributions from electron-nuclei interactions (eZ), electron-electron interactions (ee), and nuclei-nuclei interactions (ZZ). The corresponding Schrödinger equation to (2.3) does not allow an analytical solution for more than one electron, and must be solved by approximations.

A common first simplification is the Born-Oppenheimer approximation, which treats the nuclei with classical physics and invokes the adiabatic approximation. The adiabatic approximation states that electrons move on a much shorter time scale than the nuclei. Therefore, during atomic motion, the electrons instantaneously follow the nuclei without undergoing transitions between stationary states. However, the stationary states vary as the nuclei move. The adiabatic approximation holds if the ratio of the electron to nuclei mass is small, compared to the energy difference between different adiabatic eigenstates^{61 (p. 9)}. Classical treatment of the nuclei can be rationalized by their small thermal wavelengths (λ_T). λ_T is roughly the average de Broglie wavelength at a given temperature^{61 (p.10)}. Nuclei with substantially larger spacial separation than λ_T do not exhibit quantum phase coherence, and the total nuclear wavefunction is simply the product of the individual wavefunctions. H is the most difficult case, which has a thermal wavelength of about 0.2 Å at room temperature.

When the Born-Oppenheimer approximation is invoked, it is sufficient to deal with the electronic Hamiltonian \hat{H}_e :

$$\hat{H}_e = \hat{T} + \hat{V}_{\text{ext}} + \hat{V}_{ee} = \hat{T} + \hat{V}_{\text{ext}} + \hat{V}_H + \hat{V}_{XC}, \quad (2.4)$$

where \hat{T} is the kinetic energy operator for the electrons, \hat{V}_{ext} is the external classical electrostatic field set up by the nuclei, and \hat{V}_{ee} describes the electron-electron interactions. In the second equality of (2.4), \hat{V}_{ee} is split up into the classical Hartree potential \hat{V}_H and a quantum mechanical exchange and correlation potential \hat{V}_{XC} . The Hartree energy is simply the electrostatic energy of the electrons, which has a non-physical self-interaction that should be canceled by \hat{V}_{XC} .

The exchange energy stems from the indistinguishability principle and symmetrization postulate of quantum mechanics, which states that a fermionic wavefunction is anti-symmetric under particle permutation. These constraints modify the electronic energy with the so-called exchange energy. Exchange will make electrons of identical spin less likely to be close as two fermions cannot occupy the same quantum state. Correlation energy is the energy related to correlation of electronic motion. In this sense, exchange interaction is also a form of correlation.

Density Functional Theory (DFT) is based on the two Hohenberg-Kohn theorems¹⁹. The first Hohenberg-Kohn theorem states that the ground state electronic density (ρ) uniquely determines the external potential (\hat{V}_{ext}). This implies that ρ also determines the ground state $|\Psi\rangle$. The second Hohenberg-Kohn theorem defines the variational energy as a functional of ρ ¹⁹

$$E[\rho] = \langle \Psi[\rho] | \hat{T} + \hat{V}_{ee} | \Psi[\rho] \rangle + \int \rho(\mathbf{r}) v_{\text{ext}}(\mathbf{r}) d\mathbf{r} \quad (2.5)$$

Where v_{ext} is the external potential. Since \hat{V}_{ee} depends on ρ , and vice versa, the problem must be solved self-consistently.

The kinetic energy is a functional of the density, and it is unknown for the real interacting system. This difficulty is circumvented in the Kohn-Sham scheme²⁰, where the problem is mapped onto a fictitious non-interacting system, having the same density as the real system. The ground state of a non-interacting system is simply the Slater-determinant composed of the individual single particle states. In the fictitious reference system (R), the electronic Hamiltonian is^{61 (p. 61)}

$$\hat{H}_R = \sum_{i=1}^N \left(\hat{T}_R + v_R(\mathbf{r}_i) \right) \quad (2.6)$$

Where N is the number of electrons. The first term is the single particle non-interacting kinetic energy operator, and v_R is a reference potential which ensures that the density coincides with the density of the interacting system. v_R can be derived using variational calculus with the constraint that ρ integrates to N :^{61 (p. 63)}

$$v_R(\mathbf{r}) = v_{\text{ext}}(\mathbf{r}) + \int \frac{\rho(\mathbf{r}')}{|\mathbf{r} - \mathbf{r}'|} d\mathbf{r}' + \frac{\delta \tilde{E}_{XC}}{\delta \rho(\mathbf{r})}. \quad (2.7)$$

The second term in (2.7) is the Hartree potential and the third term is a chemical potential, which is formulated as a functional derivative with respect to ρ . \tilde{E}_{XC} is a modified exchange-correlation energy that must be introduced when neglecting kinetic correlations in the reference system. The Kohn-Sham equations are a set of equations defined by (2.6). These equations must be solved self-consistently as v_R depends on ρ and vice-versa. The energy is evaluated by the Kohn-Sham functional:^{61 (p. 62)}

$$E_{KS}[\rho] = T_R[\rho] + \int \rho(\mathbf{r})v_{\text{ext}}(\mathbf{r}) d\mathbf{r} + \frac{1}{2} \iint \frac{\rho(\mathbf{r})\rho(\mathbf{r}')}{|\mathbf{r} - \mathbf{r}'|} d\mathbf{r}d\mathbf{r}' + \tilde{E}_{XC}[\rho] \quad (2.8)$$

The only remaining unknown quantity is the exchange-correlation energy, which is the main determiner for the accuracy of DFT.

2.1.1 Exchange Correlation Energy Approximations

The exchange-correlation energy can be viewed as the Coulomb interaction between the density and a displaced charge density, which is brought about by exchange and correlation^{61 (p. 69)}. This displaced charge density is called the exchange-correlation hole $\tilde{\rho}_{XC}(\mathbf{r}, \mathbf{r}') = \rho(\mathbf{r}') [g(\mathbf{r}, \mathbf{r}') - 1]$. Here $g(\mathbf{r}, \mathbf{r}')$ is the pair-correlation function, describing the probability to find an electron at \mathbf{r} , given that one electron is already present at \mathbf{r}' .

The simplest and earliest kind of exchange-correlation approximation is the Local Density Approximation (LDA)²⁰. In LDA, the exchange-correlation is approximated by considering the inhomogeneous electron gas as being locally homogeneous. Thus, LDA applies the exchange-correlation hole of the homogeneous electron gas. In this way, the exchange-correlation energy is found by integration with an energy density $\tilde{\epsilon}_{XC}^{\text{LDA}}$:

$$\tilde{E}_{XC}^{\text{LDA}}[\rho] = \int \rho(\mathbf{r})\tilde{\epsilon}_{XC}^{\text{LDA}}[\rho(\mathbf{r})] d\mathbf{r}. \quad (2.9)$$

Spin-polarized systems can be treated by decomposing ρ into a spin-up and a spin-down density ($\rho = \rho_{\uparrow} + \rho_{\downarrow}$), where the Kohn-Sham equations must be solved separately for each spin channel.

LDA assumes that the energy of the system only depends on a homogeneous density at each point in space. However, for an inhomogeneous electron gas, the dependence is non-local. To introduce some semi-local behavior and improve on LDA, the Generalized Gradient Approximation (GGA) can be invoked^{61 (p. 86)}. This approximation improves over LDA by taking into account the gradient of the density. GGA functionals are constructed by augmenting the LDA energy density with an exchange-correlation enhancement factor $F_{XC}[\rho]$. The exchange-correlation energy within GGA is

$$\tilde{E}_{XC}^{\text{GGA}}[\rho] = \int \rho(\mathbf{r})\tilde{\epsilon}_{XC}^{\text{LDA}}[\rho(\mathbf{r})]F_{XC}[\rho(\mathbf{r}), \nabla\rho(\mathbf{r})] d\mathbf{r}. \quad (2.10)$$

Multiple GGA functionals have been developed, and one popular choice is the Perdew-Burke-Ernzerhof (PBE) functional⁶². Another GGA functional derived from PBE is the revised PBE functional of Hammer et al.⁶³ (RPBE), which is optimized to describe chemisorption. Metallic systems are generally well-described using PBE, whereas

chemisorption problems might prove more difficult. For example, the lattice constant of Pd is predicted to be 3.99 Å with PBE⁶⁴, and 4.02 Å using RPBE⁶³. The experimental value is⁶⁴ 3.88 Å. For chemisorption of CO on Pd(111) at the fcc site, PBE predicts⁶³ -1.94 eV, and RPBE yields⁶³ -1.65 eV. In this case, the corresponding experimental value is⁶³ -1.47 eV. This indicates that PBE performs better for the solid, whereas RPBE predicts good chemisorption energies. In microkinetic modeling, the chemisorption energies are most important as lattice-parameters do not enter the rate constant calculations explicitly. Therefore, in this thesis, the XC functional is chosen according to the chemisorption energies.

The exchange-correlation energy of GGA functionals can be improved further using different strategies⁶¹ (chap. 5) such as, meta-GGAs including the non-interacting kinetic energy density, or hybrid functionals including exact exchange energies, and van der Waals functionals. van der Waals interactions can also be included using semi-empirical pairwise atomic energy perturbations, such as D3 corrections⁶⁵.

2.1.2 Projector-Augmented Wave Method

When performing DFT calculations in practice, a certain basis set is needed to represent the Kohn-Sham orbitals. In the present work, the applied basis functions are plane waves. Plane waves are advantageous for periodic systems as they enter the Bloch theorem⁶¹ (p. 129). Another advantage of plane-waves is that increasing the basis-set size, often results in monotonous convergence of the energy. Other choices of basis functions include numerical grids and atomic orbitals⁶¹ (chap. 8).

The wavefunctions close to the nuclei oscillate rapidly due to orthogonality, and it would require an unreasonably large plane-wave basis to describe these oscillations. To avoid describing the oscillations explicitly, the Projector-Augmented Wave (PAW) method⁶⁶ is used. In PAW, the core electrons are treated as chemically frozen as they do not directly partake in the rehybridization, and only the valence electrons are treated explicitly. The valence wavefunctions are treated by introducing a linear transformation (\mathcal{T}) between the true wavefunction ($|\Psi\rangle$) and a pseudo wavefunction ($|\tilde{\Psi}\rangle$). Moreover, real-space is divided up into interstitial regions between the atomic cores and augmentation regions surrounding the cores. $|\tilde{\Psi}\rangle$ is chosen to be a smooth function inside the augmentation regions, which leads to a smaller basis set. The method requires that $|\tilde{\Psi}_i\rangle = |\Psi_i\rangle$ outside the augmentation regions, and that the wavefunctions match in value and derivative at the boundary. \mathcal{T} only acts locally in each augmentation region, and it is the identity transformation outside this region.

The transformation is performed using a different basis than plane-waves. This basis is often taken as the all-electron partial waves $|\phi_i\rangle$, which are found by integration of the radial part of the Schrödinger equation for the isolated atom. Here i entails all angular momentum quantum numbers and an index labeling the considered atom. i also contains an index n that describes different partial waves for identical angular momenta. Each $|\phi_i\rangle$ is assigned a pseudo partial wave $|\tilde{\phi}_i\rangle$, where outside the augmentation region, $|\phi_i\rangle = |\tilde{\phi}_i\rangle$. Inside the augmentation region, $|\tilde{\phi}_i\rangle$ forms a complete set. Thus, using the partial waves

as basis functions inside the augmentation regions, the transformation becomes⁶⁶

$$\begin{aligned}\mathcal{T} &= I + \sum_i \left(|\phi_i\rangle - |\tilde{\phi}_i\rangle \right) \langle \tilde{p}_i| \\ |\Psi\rangle &= \mathcal{T} |\tilde{\Psi}\rangle,\end{aligned}\tag{2.11}$$

where I is the identity operator and $\langle \tilde{p}_i|$ is a projector function. There is one $\langle \tilde{p}_i|$ for each $|\tilde{\phi}_i\rangle$, which fulfills the conditions⁶⁶:

$$\sum_i |\tilde{\phi}_i\rangle \langle \tilde{p}_i| = I, \quad \langle \tilde{p}_i | \tilde{\phi}_j \rangle = \delta_{ij}.\tag{2.12}$$

The projectors are local operators inside each augmentation region that project out the relevant part of the wavefunction. Hence, inside an augmentation region, the wavefunction is augmented by part of the sum in (2.11). Outside the augmentation region, the projectors are orthogonal to $|\tilde{\Psi}\rangle$ and no augmentation takes place.

2.1.3 Periodic Systems

The atomic model systems in the present work were mainly chosen to be periodic. The wavefunction of an electron ($\psi_{\mathbf{k}}$) in a periodic potential obeys Bloch's theorem, which can be stated as⁶¹ (p. 129)

$$\psi_{\mathbf{k}}(\mathbf{r}) = e^{i\mathbf{k}\cdot\mathbf{r}} u_{\mathbf{k}}(\mathbf{r}),\tag{2.13}$$

where \mathbf{k} is the wavevector and $u_{\mathbf{k}}$ is a function with the same periodicity as the potential. Using the periodic zone scheme⁶⁷ (p. 223) and working in the first Brillouin zone, the wavefunction of an infinite solid is described taking only one unit-cell into account. In principle, all possible wavevectors must be included in the calculation, however, in practice this is solved by Brillouin zone sampling. In Brillouin zone sampling, one represents the density, hence the energy, as a sum over special wavenumbers in the first Brillouin zone called k-points:

$$\rho(\mathbf{r}) = \sum_{\mathbf{k} \in \text{BZ}} \omega_{\mathbf{k}} \sum_{i=1}^{N_{\mathbf{k}}} f_i^{(\mathbf{k})} |\phi_i^{(\mathbf{k})}(\mathbf{r})|^2,\tag{2.14}$$

where $\phi_i^{(\mathbf{k})}(\mathbf{r})$ are the eigenstates of the Kohn-Sham equations, $f_i^{(\mathbf{k})}$ are the occupation numbers of the orbitals, $N_{\mathbf{k}}$ is the number of occupied electronic states with wavenumber \mathbf{k} , and $\omega_{\mathbf{k}}$ are weights that depend on the symmetry of the Brillouin zone. When symmetry is applied, only points in the irreducible wedge of the Brillouin zone are considered. It is necessary to solve a set of coupled Kohn-Sham equations; one for each k-point. The number of k-points is a quantity, which must be increased until convergence in some quantity of interest is achieved. A larger supercell will require fewer k-points for convergence, as a larger unit-cell results in a smaller Brillouin zone.

When calculating the density, it can be useful to work with partial occupation numbers, which is referred to as smearing of the Fermi surface. For metallic systems, this might be necessary as different k-points can make new bands enter or exit the calculation during the self-consistent solution of the Kohn-Sham equations.

2.2 Local Minimum Structures and Energies

The previous sections describe how the energy of atomic systems can be obtained given the positions of the nuclei. However, the atomic positions that correspond to local energy minima are generally not known. Energy minima are necessary to probe, as a system will spend a major part of its time near the minima. In this thesis, the main local optimization procedure is the Broyden-Fletcher-Goldfarb-Shanno (BFGS) algorithm⁶⁸. The BFGS algorithm is of the Quasi-Newton type where the atomic positions are updated according to the Hessian matrix.

In a typical calculation of a metallic system, first the bulk-material lattice constant is obtained, for example by fitting an equation of state. Next, a surface slab is constructed with a certain orientation. The number of slab-layers should be sufficiently large to converge the surface energies. Convergence can be accelerated by fixing the positions of the lowest few layers in the local optimization, to emulate a bulk surface. A plane-wave basis set enforces periodic boundary conditions perpendicular to the surface slab. Thus, a vacuum layer must be introduced to ensure that the electronic density does not overlap with its periodic repetition. To calculate adsorption energies, adsorbates are placed over sites on the surface, and the system is relaxed. There can be multiple local minima on a surface, and each possible minimum should be probed to find the lowest energy. The calculations are performed at a certain adsorbate-coverage, which in periodic calculations is determined by the simulation cell-size. For gas-phase molecules, a large cell is required to avoid interactions between periodic repetitions of the system.

Calculations for nanoparticles require choosing a specific particle shape and size. For large crystals, the shape that minimizes the surface free energy is the Wulff construction⁶⁹. However, for smaller particles, the equilibrium shapes change with size⁷⁰, for example between icosahedrons, decahedrons, and (truncated) octahedrons. In catalytic reactions, the temperature is elevated, and the lowest energy particle geometry may change dynamically¹⁴. Thus, in simulations where the particle geometry is fixed, multiple particle shapes should be investigated. This is likely most important for small particles at elevated temperatures.

After a local structural optimization is performed, vibrational energies can be calculated. This is often done by assuming a harmonic potential and finding the vibrational frequencies using finite differences. The vibrations become important when analyzing transition states, and in correcting the bare DFT energies for zero-point motion. A zero-point energy is present for confined quantum mechanical systems, as confinement lowers Δx of Heisenberg’s uncertainty principle. A small Δx implies a larger Δp , leading to zero-point motion.

2.3 Reaction Rate Constants

After the energy calculation methods have been established, rate constants can be estimated in Transition State Theory^{6;71} (TST). The TST rate constant for an elementary reaction is derived by dividing phase-space into a reactant and product region by a specific dividing surface⁷¹. All points on the dividing surface in phase-space define the transition state (R^\ddagger). Reactants (R) that cross the dividing surface become products (P). The

main assumption of TST is that the reactant and transition state are in equilibrium, and that the transition rate into the product region is sufficiently low that the Boltzmann distribution remains intact⁷¹. The second assumption is that the reactants cross the dividing surface only once. Thus, the TST estimate of the rate constant will always be larger than the actual rate constant. The reaction can be written schematically as:



The TST rate constant is expressed as an attempt-frequency ν of the molecules passing R^\ddagger into P , multiplied by the ratio of the partition functions as⁷¹:

$$k^{\text{TST}} = \nu \frac{Z^\ddagger}{Z^R}, \quad (2.16)$$

where Z^\ddagger is the partition function in the transition state and Z^R is the partition function of the reactant state. ν can be found using half the average Maxwell-Boltzmann speed $\langle v_{MB} \rangle / 2$, in the direction perpendicular to the dividing surface:

$$\nu = \frac{\langle v_{MB} \rangle}{2\delta} = \frac{1}{\delta} \frac{k_B T}{\sqrt{2\pi\mu k_B T}}, \quad (2.17)$$

where μ is an effective mass for the reaction coordinate, and δ is an assumed infinitesimal width of the transition state, such that $Z^\ddagger = \delta Z^*$. Using this, the rate constant becomes⁷¹:

$$k^{\text{TST}} = \frac{k_B T}{\sqrt{2\pi\mu k_B T}} \frac{Z^*}{Z^R}. \quad (2.18)$$

The effective mass can be interpreted by noting that $\sqrt{2\pi\mu k_B T}$ is proportional to a 1D free-translational partition function. Thus, μ allows for viewing the reaction as a translation between the initial and transition state in phase-space.

A barrierless adsorption reaction can be modeled as an ideal-gas molecule that impinges on a surface site with cross-sectional area A_{site} . The ratio of partition functions gives the relative probabilities for the TS compared to the gas-phase:

$$\frac{Z^\ddagger}{Z^R} = \frac{\delta Z^*}{Z^R} = \frac{\delta A_{\text{site}}}{V}, \quad (2.19)$$

where V is the molecular volume in the ideal-gas. Using the ideal-gas equation of state, one can use (2.18) to deduce the following expression⁷¹:

$$\begin{aligned} k_{\text{ads}}^{\text{TST}} &= \frac{A_{\text{site}}}{\sqrt{2\pi\mu k_B T}} \frac{k_B T}{V} \\ &= \frac{A_{\text{site}}}{\sqrt{2\pi\mu k_B T}} P, \end{aligned} \quad (2.20)$$

where P is the gas-phase pressure of the adsorbing species. Since the reaction coordinate is a free translation, μ is the molecular mass (M), and the rate constant coincides with the expression from collision theory (apart from a sticking probability):

$$k_{\text{ads}} = \frac{A_{\text{site}} s_0}{\sqrt{2\pi M k_B T}} P, \quad (2.21)$$

where A_{site} is the area of one adsorption site, and s_0 is the sticking coefficient. If this expression is used for the adsorption rate constant, the corresponding desorption rate constant k_{des} can be determined from the equilibrium constant K :

$$K = \frac{k_{\text{ads}}}{k_{\text{des}}} = e^{\frac{-\Delta G}{k_{\text{B}}T}}, \quad (2.22)$$

where ΔG is the Gibbs free energy change upon adsorption. In this manner, thermodynamic consistency is ensured. Using equilibrium constants to calculate desorption rate constants ensures that the elementary-step rates are reasonable. However, the procedure is not assuming the elementary-step to be in equilibrium over the entire surface from the beginning of the simulation.

For reactions occurring on the surface, the reaction coordinate is often assumed to be a harmonic vibration with frequency ν , which is equal to the attempt frequency in (2.16). Assuming that the TS-mode along the reaction coordinate is low in vibrational energy ($h\nu \ll k_{\text{B}}T$), the classical limit can be taken, where the vibrational partition function is $\frac{k_{\text{B}}T}{h\nu}$. The rate constant can be derived as⁶:

$$k^{\text{TST}} = \frac{k_{\text{B}}T}{h} \frac{Z^{\text{TS}}}{Z^{\text{R}}}, \quad (2.23)$$

where Z^{TS} is the transition state partition function, for the transverse degrees of freedom with respect to the reaction coordinate. Calculating both partition functions in the harmonic approximation and working with (2.23), is referred to as harmonic transition theory. In harmonic transition state theory, the effective mass is not needed. However, comparing (2.18) to (2.23), the effective mass is identified as

$$\mu = \frac{k_{\text{B}}T}{2\pi\nu^2\delta^2}. \quad (2.24)$$

2.4 Energy Barriers with Nudged Elastic Band Calculations

The free energy barrier for moving a system from the initial state to the transition state largely determines the rate constants. Identifying transition states is therefore a critical task. Nudged Elastic Band⁷² (NEB) is a method to identify transition states by finding the Minimum Energy Path (MEP) between an initial state and final state.

To set up a NEB calculation, the initial and final atomic positions are specified. Next, the atomic positions are interpolated between the initial and final state. The resulting atomic configurations are called images, and the distance between each image is described by a reaction coordinate r . The total force on each image is decomposed into parallel (F_{\parallel}) and perpendicular (F_{\perp}) components as:

$$F = F_{\parallel} + F_{\perp} = -kr + F_{\perp} \quad (2.25)$$

where k is a spring constant. Hence, each image interacts with its neighbor images parallel to the MEP by spring-forces. To find the MEP, structural relaxation is performed on

each image. F_{\parallel} prohibits full relaxation of each image down to a local minimum, e.g. the initial or final state. F_{\perp} ensures that each image relaxes towards the MEP at the given reaction coordinate. In this manner, the images are stretched like an elastic band along the MEP.

After a coarse initial simulation, the highest energy image should be released from all spring forces, and F_{\perp} should be reversed. This procedure is called the Climbing Image method⁷². The CI method helps finding the highest point on the MEP, as the image climbs up the MEP to the maximum energy point. If the maximum energy image has one imaginary vibration frequency parallel to the MEP, the point is a saddle on the PES. Typically, this saddle point is chosen to represent the transition state that separates reactants and products in phase-space.

2.5 Adsorbate-Adsorbate Interactions

The adsorbates on a catalyst interact either by direct interactions or through the surface^{73;74}. Such phenomena can have large effects on the binding energies of certain species and consequently may be important for the kinetics. Kinetic simulations need to take these interactions into account by modifying the reaction energies as a function of the adsorbate configurations. When doing this, care must be taken to preserve thermodynamic consistency.

Adsorbate-adsorbate interactions can be implemented as functions of the adsorbate coverages. Following this method, the energies are perturbed using the differential adsorption energies as a function of the coverages. It is important to use the differential adsorption energies instead of the average adsorption energies, as adding another adsorbate will alter the energy of the system based on the adsorbates that are already present. Adsorbate-adsorbate interactions can also be fitted to specific atomic arrangements. A systematic method to calculate interactions is using cluster expansion Hamiltonians⁷⁵ (p. 94), where a Hamiltonian is fitted to certain geometric occupation-patterns. The expansion is truncated at a certain number of nearest neighbor distances, and typically including two and three-particle interactions. In the current work, only the first nearest-neighbor interactions, including two-particle interactions, are considered. This approach should capture the main effects of the interactions. However, it is meaningful for future work to further explore the limitations of this simple approach.

The adsorbate-adsorbate interactions influence the kinetics significantly. For example, Figure 2.1 shows simulated coverages as a function of temperature for complete methane oxidation over Pd(100) using the microkinetic model of **Paper IV**. The applied model includes O-O, C-C, and OH-OH interactions. The figure shows coverages when the interactions are turned off and are at full strength. Without any interactions, O is poisoning the surface with a very high coverage, and there is no space for C. At full interaction strength, there is a coverage of both C and O. This difference in coverages can modify the rates by several orders of magnitudes, and it can also change the dominating reaction paths. Thus, including adsorbate-adsorbate interactions are of utmost importance for obtaining reasonable coverages and kinetics.

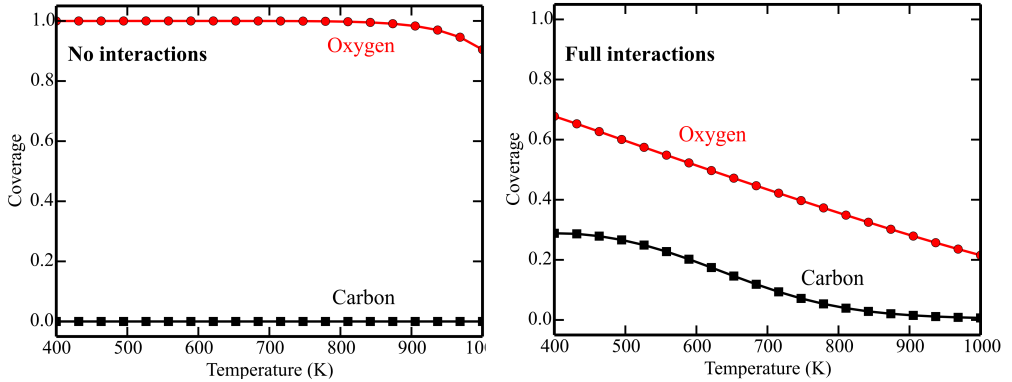


Figure 2.1: Simulated coverages without adsorbate-adsorbate interactions (left) and with adsorbate-adsorbate interactions (right) during complete methane oxidation over Pd(100). Pressures: 0.61 mbar methane and 3.06 mbar oxygen.

2.6 Modeling Entropy in Catalytic Reactions

Adsorbate entropies must be considered as they enter the Gibbs free energy. Typically, entropy is modeled in the canonical ensemble, using the canonical partition function (Z). Z is a sum over all states, available to the system. The entropy and partition function of a system are related by the connection between statistical mechanics and thermodynamics⁷⁶

$$S = -\frac{\partial}{\partial T} (-k_B T \ln Z)_{V,N} = k_B \ln Z + k_B T \frac{1}{Z} \left(\frac{\partial Z}{\partial T} \right)_{V,N} \quad (2.26)$$

2.6.1 Gas-phase Molecules

For an ideal-gas molecule, the potential energy landscape of translation is flat, and the translational, rotational, and vibrational degrees of freedom are decoupled. Thus, the total partition function is a product of free translations, rotations, and vibrations as:

$$Z = Z^{\text{trans}} Z^{\text{rot}} Z^{\text{vib}}. \quad (2.27)$$

The translational part of the partition function of the free-gas molecule is given by^{2 (p. 89)}

$$Z^{\text{trans}}(V) = V \left(\frac{2\pi M k_B T}{h^2} \right)^{3/2}, \quad (2.28)$$

where V is the molecular volume of the gas, and M is the mass. V is often substituted for the pressure using the ideal gas equation of state $pV = k_B T$. The ideal-gas (free) rotational partition-function can be calculated in the rigid-rotor approximation, which for non-linear molecules gives^{2 (p. 92)}:

$$Z_{\text{non-linear}}^{\text{rot}} = \frac{1}{\sigma} \left(\frac{8\pi^2 k_B T}{h^2} \right)^{3/2} \sqrt{\pi I_A I_B I_C}, \quad (2.29)$$

where I_X is the moment of inertia of the molecule around the principal axis X , and σ is the symmetry factor of the molecule. For a linear molecule, the rigid rotor partition function is

$$Z_{\text{linear}}^{\text{rot}} = \frac{1}{\sigma} \left(\frac{8\pi^2 k_B T}{h^2} \right) I. \quad (2.30)$$

Finally, the vibrations are bound by a potential, which can be modeled in the harmonic approximation to yield² (p. 90)

$$Z^{\text{vib}} = \prod_i \frac{e^{-\frac{h\nu_i}{2k_B T}}}{1 - e^{-\frac{h\nu_i}{k_B T}}}, \quad (2.31)$$

where ν_i is the vibrational frequency of mode number i . The harmonic approximation assumes that the molecule is subject to a quadratic potential leading to the harmonic oscillator energies $h\nu_i$, which can be calculated using finite differences in the energies obtained with DFT.

2.6.2 Adsorbates

The partition function of adsorbates differs from gas-phase molecules. This is owing to the different potential energy landscapes for adsorbate translation, rotation, and possibly vibration. Typically, translations give the largest contribution to the entropy, rotations the next largest, and vibrations yield the smallest contribution. Thus, modeling translational modes should be first priority when calculating entropy. The simplest approximation is to assume that the molecule is free to translate over the surface, as a free 2D gas. This can be reasonable for loosely bound molecules⁷⁷. In this free translator model, adsorbates are free to translate over an area⁷⁸. The area is ideally determined by the equilibrium surface-coverage. However, the equilibrium coverage depends on the entropy, and should strictly be determined self-consistently. This problem has been addressed by defining a standard state for the surface coverage⁷⁹. However, the standard-state approach assumes that the adsorbate is an ideal 2D gas, and should be viewed as an approximation. Another simple approximation is to determine the free area by evaluating the entropy near the expected equilibrium coverage. The partition function in the free translator, for the two surface-parallel translational degrees of freedom partition is:

$$Z_{\text{free}}^{\text{trans-2D}} = A \frac{2\pi M k_B T}{h^2}, \quad (2.32)$$

where A is the area that the adsorbate is free to translate over. The free translator defines an upper bound to the translational entropy of any adsorbate as it corresponds to a completely flat potential energy landscape. The remaining degrees of freedom are assumed to be frustrated vibrations using (2.31).

While the free translator is simple, the most common approximation is the harmonic approximation, where all adsorbate degrees of freedom are assumed to be independent frustrated vibrations^{46;78;80}. In this case, the full partition function is described by (2.31).

This tacitly assumes that the adsorbate binds to only one adsorption site. If low-energy modes are present ($< 100 \text{ cm}^{-1}$), it can be necessary to truncate the value, as low-energy modes are computationally uncertain.

Kinetic models generally need to work over a range of temperatures. The free translator might be correct at high temperatures, and the harmonic approximation at low temperatures, depending on the diffusion barriers. To capture this behavior, the hindered translator/rotor model^{78;81} can be used. The hindered translator includes the diffusion barriers of the adsorbates in the partition function. The model is simple as it approximates the surface topology by only treating the fastest path of diffusion. The adsorbate is considered in a sinusoidal potential, where the 2D surface-parallel partition function becomes⁷⁸:

$$Z_{\text{HT}}^{\text{trans}} = \frac{N_{\text{sites}} \frac{\pi r_x}{T_x} \exp\left(-\frac{r_x + 1}{T_x}\right) I_0^2\left(\frac{r_x}{2T_x}\right)}{\left[1 - \exp\left(-\frac{1}{T_x}\right)\right]^2} \exp\left(\frac{2}{(2 + 16r_x)T_x}\right). \quad (2.33)$$

$T_x = k_{\text{B}}T/h\nu_x$ is the ratio between the thermal energy and the vibrational energy, and $r_x = W_x/h\nu_x$ is the ratio between the diffusion barrier W_x and the vibrational energy. N_{sites} is the number of surface sites, and I_0 is the zero-order modified Bessel function of the first kind, arising from the periodic potential. The last exponential in (2.33) accounts for zero-point energy corrections⁷⁸. There are some uncertainties in working with the hindered translator. For example, it treats surface symmetry in a rough way by assuming that the potential energy surface for diffusion is a linear function [$U(x, y) = U(x) + U(y)$], which is questionable for surfaces without square symmetry. The hindered translator can, however, be expected to be quite accurate for closed-shell molecules, due to the presumably flat energy landscape for diffusion.

The harmonic approximation, free translator, and hindered translators are the most commonly applied entropy models. However, these models are approximate, and do not necessarily capture the entropy of the specific potential energy surface. As an alternative, we developed the Complete Potential Energy Sampling (CPES) method in **Paper I**. CPES calculates the adsorbate entropy numerically by sampling the potential energy surface. The vibrational and rotational degrees of freedom were treated as frustrated vibrations using (2.31), and the 2D translational partition function was numerically calculated by DFT. It is reasonable to treat the translations explicitly, as translations are by far the largest contribution to the entropy. The 2D translational partition function was derived to be:

$$Z_{\text{CPES}}^{\text{trans}} = \frac{2\pi M k_{\text{B}}T}{h^2} \iint \exp\left[\frac{-U(x, y)}{k_{\text{B}}T}\right] dx dy, \quad (2.34)$$

where $U(x, y)$ is the potential energy of the molecule at position (x, y) in the unit-cell. $U(x, y)$ is calculated with DFT by locally optimizing the adsorbate in the direction perpendicular to the surface, for various (x, y) . The partition function (2.34) is seen to be the free translational partition function, multiplied by an integral over potential energy surface for adsorbate translation. Thus, the potential energy is assumed to give rise to a Boltzmann distribution of the momenta. The partition function (2.34) approaches the free

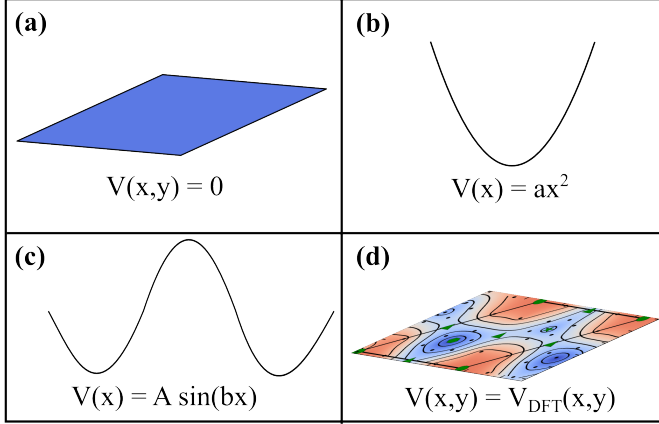


Figure 2.2: Schematic illustration of the potential energy landscape for translation in (a) the free translator model, (b) the harmonic approximation, (c) the hindered translator model, and (d) CPES.

translator (2.32) in the limit of a flat potential [$U(x, y) \rightarrow 0$]. Moreover, (2.34) becomes the hindered translator when applying a sinusoidal potential. Thus, the developed CPES method includes all the approximate models. CPES has the possibility to be more accurate as it is only limited by the accuracy of the DFT calculations. The CPES method was later extended to include zero-point corrections⁸², which can be important at very low temperatures. The four discussed models of entropy are summarized in Figure 2.2.

CPES can directly numerically integrate 2D potential energy surfaces. However, the more complicated case of a 3D potential energy surface is important, for example, when modeling reactions in zeolites. In **Paper II**, we extended CPES to model the entropy of molecules diffusing in zeolite pores, which is a challenging problem that has attracted large interest^{83–86}. The molecules in zeolites show a 3D restricted gas-like behavior, as we observed by Molecular Dynamics (MD) simulations. In the simulations, the molecule collided frequently with the framework, which requires that the translational and rotational partition functions are modeled as coupled. It is noteworthy that the mean-free path of the molecule in the true gas-phase is much larger than the zeolite pore-dimension. For example, for a gas of N_2 at 1 mbar and 473 K, the mean-free path is ca. 0.2 mm, which is 10^6 times the cage diameter in chabazite (a small pore zeolite). Monte Carlo integration was used to evaluate the semi-classical partition function:

$$Z^{\text{CPES}} = Z^{\text{vib}} Z_{\ell}^{\text{rot}} \frac{Z^{\text{trans}}(V)}{V} \int \exp \left[\frac{-U(\mathbf{r}, \Phi)}{k_B T} \right] d\mathbf{r} d\Phi, \quad (2.35)$$

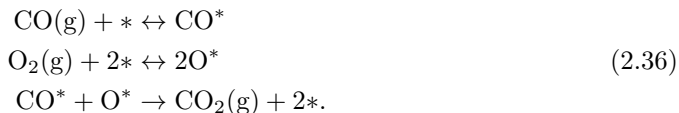
where \mathbf{r} is the center of mass position of the molecule and Φ is a generalized coordinate that describes molecular rotations. The partition functions that are multiplied onto the integral are the free-gas partition functions, which again reflects the Boltzmann distribution of the (conjugate) momenta, determined by the potential energy surface. The investigated molecules (N_2 and CH_4) are calculated to lose 1/3-1/2 of their gas-phase entropy upon adsorption, which suggests that the entropy is ill-described for both

the harmonic approximation and free translator. The result we obtained of losing 1/3-1/2 of the gas-phase entropy is a slightly more detailed result than previous heuristic estimates, where the molecules were assumed to lose one or two full translational degrees of freedom^{84;87}.

The approximations discussed in this section do not include adsorbate-adsorbate interactions, which may affect the entropy. CPES can include adsorbate-adsorbate interactions by reformulating (2.34) or (2.35) as a multi-dimensional integral over the molecules and mapping out a potential energy surface $U(\mathbf{r}_1, \mathbf{r}_2, \dots, \Phi_1, \Phi_2, \dots)$.

2.6.3 Influence of Entropy in Kinetics

First-principles microkinetic models have typically described adsorbate-entropies in the harmonic approximation^{46;78;80}. Moreover, weakly bound adsorbates have previously been treated as losing one, or all, translational degrees of freedom upon adsorption^{45;88-90}. This thesis takes a step towards more accurate kinetic simulations, by investigating explicitly how more detailed entropy models affects kinetics. CO oxidation over Pt(111) was used as an archetype reaction. CO oxidation has the advantage that the reaction is well-studied^{45;91-99}, which enables detailed comparison to experiments. The reaction was modeled in the mean-field approximation (see Chapter 3) using a Langmuir-Hinshelwood mechanism^{45;91;94-96;99;100}:



For all investigated models, the entropies of CO and O were found to be different. CO translates on a flat potential energy surface with low diffusion barriers, which results in a high entropy. O instead clearly prefers fcc binding and has high diffusion barriers, which results in a low entropy. This can be important as mean-field models usually include only a generic and coarse-grained site, which does not describe the detailed nature of the site. The coarse-grained site could entail fcc, hcp, ontop, and bridge sites. When the adsorption energies on these sites are similar, the translational entropy can be high and should be modeled accordingly.

The lowest entropy is predicted by the harmonic approximation, which for CO lies about 0.4 meV/K lower than the CPES result. At 500 K, this corresponds to 0.2 eV, which can be considered a significant difference. For O, the harmonic approximation is much better suited and lies close to the CPES entropy. To quantify the significance of the entropy difference, Figure 2.3 compares the light-off temperature ($T_{1/2-\text{max}}$) of the four entropy models to experimental data^{91;93;96;99}. The harmonic approximation and free translator under and overestimate the light-off temperature, respectively. The hindered translator and CPES agree well with the experimental references, over the entire pressure-range. Hence, modeling the entropy in detail moves the results significantly closer to experimentally obtained values. The effect of entropy on kinetics is readily understood by noting that a high entropy implies a lower adsorbate free energy.

The overall conclusion from the work on entropy is that treatment of adsorbate entropy can affect kinetic simulations significantly. Whether entropy should be modeled

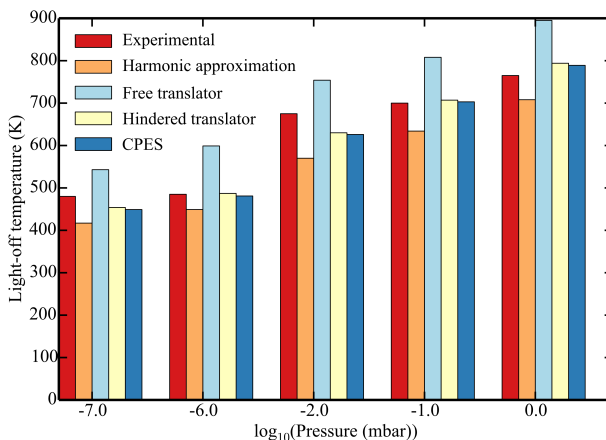


Figure 2.3: Simulated and experimental light-off temperature as a function of pressure. The experimental references are: Campbell et al.⁹¹ (10^{-7} mbar), Vogel et al.⁹⁶ (10^{-6} mbar), Nakao et al.⁹³ (10^{-2} mbar), and Calderón et al.⁹⁹ (10^{-1} - 10^0 mbar).

with high accuracy or not depends on the desired level of detail. For more qualitative studies, it is likely sufficient to capture the nature of the degrees of freedom. Moreover, mobile molecules should not be modeled in the harmonic approximation. Potential energy sampling is particularly important in zeolites where the degrees of freedom are coupled and are far from harmonic.

Summary

This chapter has described rate constant calculations from first principles. The rate constants depend on Gibbs free energy changes, which are determined by reaction energy barriers, adsorbate-adsorbate interactions, and entropy changes. The uncertainties in calculating rate constants primarily come from the accuracy of the DFT calculations, the approximate treatment of adsorbate-adsorbate interactions, and modeling of entropy. DFT calculations and adsorbate-adsorbate interactions give a large contribution to the uncertainty, whereas entropy has a slightly lower impact.

Chapter 3

Methods of Kinetic Modeling

The present chapter deals with simulating and analyzing reaction kinetics. Reaction kinetics is important to investigate as it provides important insights into the main reaction mechanisms and performance bottlenecks.

3.1 Chemical Master Equation

The reaction kinetics of a system is a set of transitions between various chemical states, occurring on a high-dimensional free energy surface, separated by several maxima and minima. In principle, reactions can be followed in space and time by solving the Newtonian equations of motions with molecular dynamics. However, molecular dynamics is unfeasible for simulations of reaction kinetics, because the time-scale of vibrations is several orders of magnitude smaller than the typical time of a chemical reaction.

The chemical master equation takes advantage of the time-scale separation between vibrations and chemical reactions by solely describing chemical transitions. This is done by dividing phase-space into regions corresponding to different chemical states of the system. Let α and β denote the states of the system. The chemical master equation for α involves a sum over all states β , which can bring the system into α :^{75 (p. 31)}:

$$\frac{dP_\alpha}{dt} = \sum_{\beta} [W_{\alpha\beta}P_\beta - W_{\beta\alpha}P_\alpha], \quad (3.1)$$

where $W_{\alpha\beta}$ is the transition rate from β to α , and P_α is the probability for the system to be in α . One equation exists for each α , and the master equation should be viewed as a set of coupled differential equations. In practice, the state is often defined by the coverages on the catalyst sites:

$$\alpha \sim \{A^*, B^*, *, *, A^*, *, A^*, B^*, \dots\}, \quad (3.2)$$

where A and B are chemical species, and $*$ denotes an empty site, such that the set describes the site-occupations. The chemical master equation is the key to the kinetics of the system as it describes the time-evolution for the probability of observing the states. A high transition rate into a particular state and a low transition rate out of the state implies that its probability increases in time. Thus, the kinetics will follow a set of transitions towards a set of most probable states, which defines the equilibrium. At equilibrium $\frac{dP_\alpha}{dt} = 0$, which is enabled by $W_{\alpha\beta}P_\beta = W_{\beta\alpha}P_\alpha$. This is known as the principle of detailed balance, which reflects that each event is in equilibrium with its own inverse. The chemical master equation can be solved using either the stochastic kinetic Monte Carlo technique or approximately in the mean-field picture.

3.2 Mean-Field Approximation

The Mean-Field Approximation (MFA) yields an approximate solution to the chemical master equation. An advantage of the MFA is that it focuses on the average behavior of the system by describing the coverages, which makes the results simple to analyze. The computational cost of the MFA is considerably smaller than kinetic Monte Carlo simulations, as the mean-field equations often can be solved on a desktop computer within some minutes. MFA has the disadvantages of assuming infinite surfaces with only one type of site, and a completely random adsorbate-distribution. These assumptions hinder proper description of nanoparticles. Moreover, the adsorbate-distribution is not random in the presence of adsorbate-adsorbate interactions. The situation is particularly severe for attractive interactions that lead to pairing of adsorbates; an effect that can be critical for some reactions⁴⁹. Although the MFA breaks down for significant adsorbate-adsorbate interactions, it is common practice to include interactions to obtain reasonable steady-state coverages.

For a simple elementary reaction step, the MFA can be derived as follows. Consider a model surface reaction between species A and B : $A + B \rightarrow AB$. The average number of species A on the surface is given as a weighted average over the states as:^{75 (p. 105)}

$$\langle N_A \rangle = \sum_{\alpha} P_{\alpha} N_{\alpha}^{(A)}, \quad (3.3)$$

where $N_{\alpha}^{(A)}$ is the number of species A in state α . Inserting (3.1) into (3.3), and rearranging the indices of summation yields^{75 (p. 111)}:

$$\frac{d\langle N_A \rangle}{dt} = \sum_{\alpha} \sum_{\beta} \left[N_{\alpha}^{(A)} - N_{\beta}^{(A)} \right] P_{\beta} W_{\alpha\beta}. \quad (3.4)$$

When the reaction $A^* + B^* \rightarrow AB^*$ proceeds, one A is consumed, and $N_{\alpha}^{(A)} - N_{\beta}^{(A)} = -1$. Moreover, for each β , the number of terms in the sum having non-zero $W_{\alpha\beta}$ is equal to the number of neighboring (A, B) pairs on the surface $[N^{(AB)}]$. Using this, and assuming that the transition rates for all terms are W , expression (3.4) becomes^{75 (p. 112)}:

$$\frac{d\langle N_A \rangle}{dt} = \sum_{\beta} -P_{\beta} W N_{\beta}^{(AB)} = -W \langle N^{(AB)} \rangle. \quad (3.5)$$

If the adsorbates are randomly distributed over a homogeneous surface, the number of pairs becomes^{75 (p. 112)}:

$$N_{\beta}^{(AB)} = Z N_{\beta}^{(A)} \frac{N_{\beta}^{(B)}}{S-1}, \quad (3.6)$$

where Z is the number of nearest neighbors of a site, and S is the number of surface sites. The factor $N_{\beta}^{(B)}/(S-1)$ is the probability for a site to be occupied by B . Inserting (3.6) into (3.5) gives:

$$\frac{d\langle N_A \rangle}{dt} = -\frac{WZ}{S-1} \langle N^{(A)} N^{(B)} \rangle. \quad (3.7)$$

The mean of the product is rewritten as the product of the means, augmented with the fluctuations from the individual means:

$$\langle N^{(A)} N^{(B)} \rangle = \langle N^{(A)} \rangle \langle N^{(B)} \rangle + \langle [N^{(A)} - \langle N^{(A)} \rangle] [N^{(B)} - \langle N^{(B)} \rangle] \rangle. \quad (3.8)$$

In the limit of an infinite number of sites, $S - 1 \approx S$, and when neglecting fluctuations, (3.7) becomes

$$\frac{d\langle N_A \rangle}{dt} = -\frac{WZ}{S} \langle N^{(A)} \rangle \langle N^{(B)} \rangle. \quad (3.9)$$

Dividing by the total number of sites, the mean-field equation is found for the time-evolution of A :

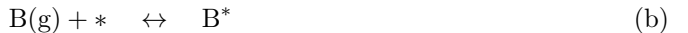
$$\frac{d\theta_A}{dt} = -k\theta_A\theta_B, \quad k = WZ, \quad (3.10)$$

where θ_i is the coverage of species i on the surface, and k is identified as the rate constant of the reaction. Similar equations can be derived for θ_B , θ_{AB} , and the fraction of empty sites. For multiple reactions, each reaction contributes to $\frac{d\theta_A}{dt}$ with a similar term, owing to the linearity of the master equation. As the adsorbate distribution is assumed random, θ_A corresponds to the probability for having species A on a surface site. The random adsorbate distribution implies that configurational entropy is implicitly described in the mean-field equations.

In practice, mean-field models are constructed by a list of coverages ($\boldsymbol{\theta}$) for species that may cover the surface, and a set of reactions with rates $R(\boldsymbol{\theta})$. From this information, a system of coupled first-order ordinary differential equations is formulated:

$$\frac{d\theta_i}{dt} = \sum_j c_{ij} R_j(\boldsymbol{\theta}), \quad (3.11)$$

where c_{ij} is an integer that describes how many i -species that are produced in reaction j . R_j is the rate of the elementary reaction j , which is equal to the rate constant multiplied by the relevant coverages. As an example of deriving the mean-field equations, consider the following schematic reaction:



The time-evolution of the coverage of A is given by:

$$\frac{d\theta_A}{dt} = 2k_a^+ \theta_*^2 - 2k_a^- \theta_A^2 - k_c^+ \theta_A \theta_B \quad (3.12)$$

where k_i^\pm are the rate constants for reaction i , and $*$ indicates an empty site. The first term comes from the forward-reaction of (a), which requires two sites for dissociation such that θ_* enters squared. The factor two is present as two A are formed upon adsorption. The second term stems from the backward reaction of (a), and is negative as A is consumed

by the elementary step. The third term arises from reaction (c), which requires one A and B . For species B , the coverage equation is:

$$\frac{d\theta_B}{dt} = k_b^+ \theta_* - k_b^- \theta_B - k_c^+ \theta_A \theta_B. \quad (3.13)$$

The resulting system of differential equations is often solved numerically. In the present work, this is performed using SciPy¹⁰¹. Before integration, the initial conditions are specified, which is important as different initial conditions can lead to different steady-states. The steady-state is reached when all coverages are constant in time. A common situation is that the rate constants vary by several order of magnitudes, which makes the equations stiff. Therefore, an integration method that handles stiff problems must be chosen, and in the present work the backward differentiation formula¹⁰² method was found to be most effective.

3.3 Kinetic Monte Carlo

Kinetic Monte Carlo¹⁰³ (kMC) is a stochastic method to solve the chemical master equation. KMC has the advantage over the MFA that it enables investigations of more realistic systems. This is primarily owing to the assumptions in MFA of random adsorbate distributions and the infinitely large surface. A nanoparticle is an example of a finite system with specific adsorbate patterns, where kMC must be used. KMC simulations have the disadvantages that the results are more complex to analyze, and the computational cost is significantly higher than in the MFA.

In kMC, the system starts in a specific state that, with time, transitions into different states, governed by random number generation. KMC solves the master equation by simulating the transitions between states as a function of time. This is done by simulating a large number of reaction events and their time of occurrence. The kMC method can be implemented using various algorithms, for which two popular choices are the Variable Step Size Method (VSSM), also known as the n-fold way¹⁰⁴, and the First-reaction method (FRM)⁷⁵ (Chap. 3). In the present work, the shortest computational time is obtained using the FRM algorithm. Before performing a simulation, the types of possible reactions are defined. When this is done, FRM can be performed by an algorithm that is summarized in Figure 3.1.

- **Step 1:** The simulation is initialized by setting time $t = 0$, defining when the simulation should end (t_{end}), choosing the reaction conditions, and initializing the site occupations. Here, an event-list is initialized to keep track of possible reactions events, their time of occurrence, and the site where they proceed. The event-list is updated at each simulation step.
- **Step 2:** For all possible events, the times of occurrence are generated, and the event-list is populated. The time of occurrence $t_{\beta\alpha}$ for taking the system from state α to state β is calculated according to⁷⁵ (p. 53)

$$t_{\beta\alpha} = t - \frac{1}{W_{\beta\alpha}} \ln u \quad (3.14)$$

Where t is the current simulation time, $W_{\beta\alpha}$ is the rate constant of the event, and u is a random uniform number in the interval $]0, 1]$.

- **Step 3:** Determines whether the simulation has ended by checking if $t \geq t_{\text{end}}$.
- **Step 4:** Performs the chronologically next reaction in the event-list. If the next reaction is impossible, it is discarded and the next possible event is performed.
- **Step 5:** The event-list is updated by adding new events made possible by the last simulation step. This is only done in a neighborhood around the site where the last event happened, since avoiding globally updating saves a significant amount of computational resources for large systems.
- **Step 6:** Defines the end of the simulation, where quantities of interest are saved. To lower the memory consumption, saving data and cleaning different lists should also be done during the simulation.

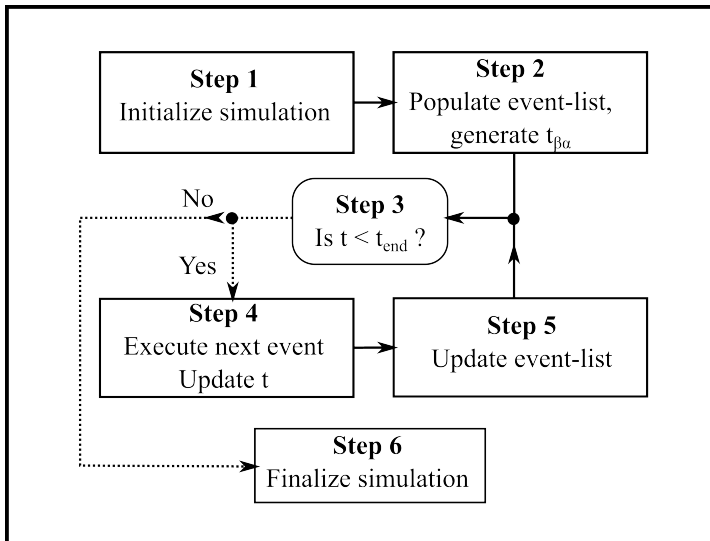


Figure 3.1: A flowchart of the first reaction method of kinetic Monte Carlo.

The sites and their mutual connectivity must be given a representation in kinetic Monte Carlo simulations. The conventional approach is to perform the simulations on a lattice^{105–110}. A more detailed and flexible approach is to use graph-theory to define a global connectivity pattern^{110;111}. In the present work, the sites were represented by nearest neighbor lists, as described in **Paper III**. With this approach, the set of all the neighbor lists gives the global connectivity pattern, similar to graph-theory. The implemented neighbor-list approach has an advantage over a lattice-based approach, as incommensurate lattices and dynamical catalyst changes can be accounted for in a simpler manner. A useful way to save computational resources and simplify the simulations is

to coarse grain the sites to entail multiple adsorbate binding positions, such as hollow, bridge, and ontop positions. This approach was followed in this thesis.

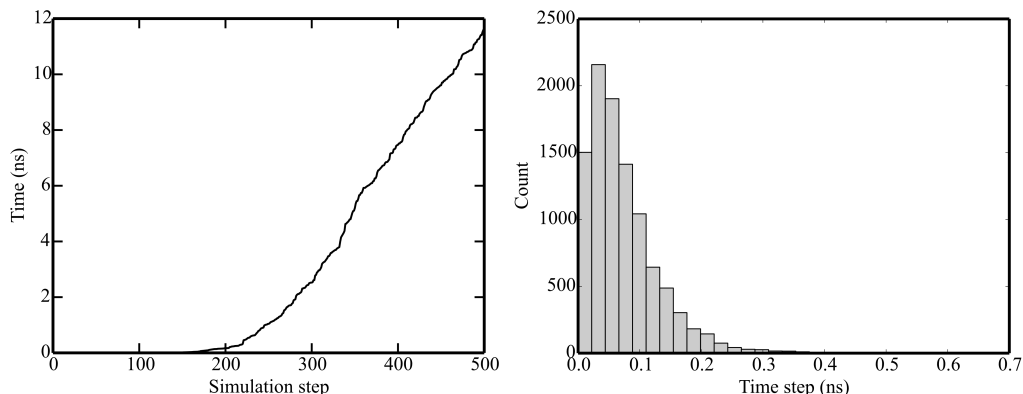


Figure 3.2: Time evolution in kinetic Monte Carlo simulations of CO oxidation on a 5.2 nm Pt nanoparticle. Left: Time as a function of simulation step. Right: A histogram over the time step. Reaction conditions: 600 K, 20 mbar CO, and 10 mbar O₂. The CO diffusion barrier is increased from 0.08 to 0.58 eV.

The time-step in the simulations is governed by the rate of the fastest reactions as these events are executed with the highest probability. Figure 3.2 (left) shows time as a function of simulation step during a short Monte Carlo simulation of CO oxidation over a Pt nanoparticle. The time increment is small in the beginning of the simulation, and becomes larger as the simulation proceeds. This occurs as the fastest rates decrease in speed when approaching equilibrium. Figure 3.2 (right) shows a histogram over the time-step. The shortest time-steps are mostly originating from the beginning of the simulation, where the reaction is far from equilibrium. The histogram resembles an exponential distribution, which is reasonable as the events essentially are Poisson processes.

Catalysts operate over long time scales, however, the time evolution of a simulation is instructive to consider. Figure 3.3 shows the CO coverage on a nanoparticle during a short simulation of the CO oxidation reaction. At 600 K (left), the facets contain free sites, whereas the edges and corners are completely filled. At 1200 K (right), the coverages on the edges are lower, whereas the corners and facets are empty. One interesting observation is that there are large fluctuations in the coverages, which are most pronounced for the low-coordinated sites, as they are less abundant. The magnitude of the fluctuations increases with temperature and are magnified for smaller systems. Mean-field models assume that fluctuations can be neglected, which is questionable considering the results in Figure 3.3.

3.3.1 Observing Rare Events

A significant challenge in kMC is that the fastest reactions determine the time-step. Diffusion can often be several orders of magnitudes faster than chemical transitions, which renders kMC impractical for catalytic reactions. A particularly simple solution is to

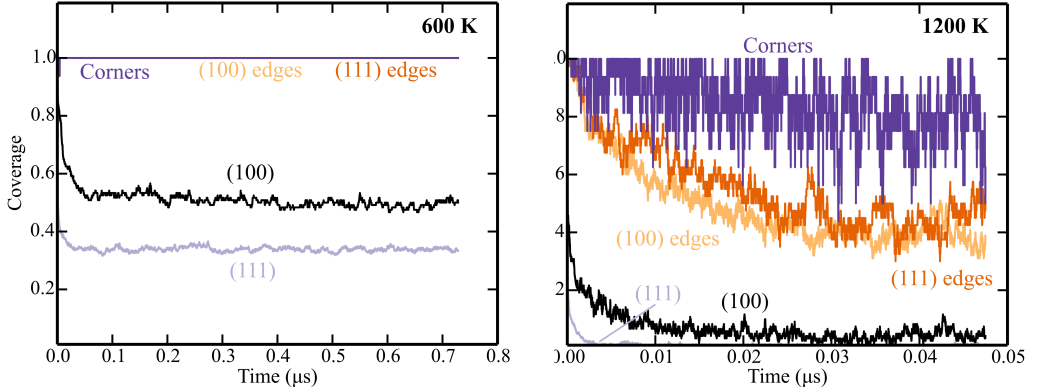


Figure 3.3: Simulated CO coverage in CO oxidation on a 5.2 nm Pt nanoparticle at temperature 600 K (left) and 1200 K (right). Pressures: 20 mbar CO and 10 mbar O₂. The CO diffusion barrier is increased from 0.08 to 0.58 eV.

permanently slow down the fast reactions⁷⁵ (pp. 162-163). This must be done while ensuring that the fast events remain quasi-equilibrated. A more detailed approach uses the concept of superbins. A superbins is defined as a set of configurations that are connected by quasi-equilibrated elementary steps, and consequently are revisited often^{113–115}. The superbins-configurations are connected by fast events, which can be slowed down to escape the superbins. This method can, however, be computationally expensive as it involves logging and revisiting a huge number of configurations.

An efficient method is the generalized temporal acceleration scheme¹¹², where entire groups of quasi-equilibrated events are slowed down, periodically. During simulation, the forward and backward rates of each reaction-type determine if the reaction is quasi-equilibrated. Reactions that are flagged as quasi-equilibrated once, keep this tag for the entire simulation. If quasi-equilibrated events are executed, the system remains in the superbins, whereas non-equilibrated events exit the superbins. The concept is sketched in Figure 3.4, where the superbins, at a certain time, is divided into an explored and unexplored region. The average rate of each possible reaction is calculated by summing over the observed configurations in the superbins¹¹²:

$$r_m = \frac{1}{\sum_{n \in S} \Delta t_n} \sum_{n \in S} k_m(x_n) \Delta t_n, \quad (3.15)$$

where Δt_n is the time spent in configuration x_n , and $k_m(x_n)$ is the rate constant of reaction m in x_n . The estimated escape-time from the currently explored region of the superbins is given by¹¹²:

$$\tau_s^{-1} = R_s = \sum_{m \in N, Q_B} r_m, \quad (3.16)$$

where the sum runs over non-equilibrated and insufficiently executed quasi-equilibrated events, and R_s is the escape-rate from the currently explored region. A quasi-equilibrated

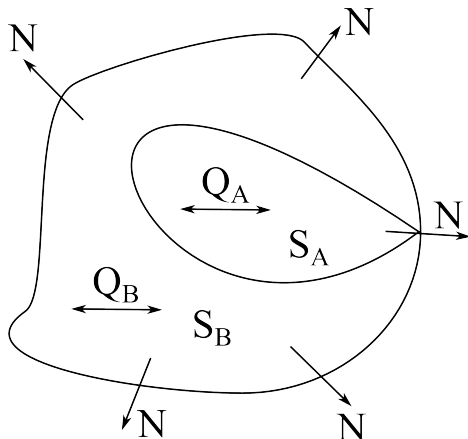


Figure 3.4: Sketch of the superbasis principle. The explored region of the superbasis (S_A) is connected by the set of events Q_A , and the unexplored region (S_B) is connected by the set Q_B . The system can leave S_A or S_B via non-equilibrated events N . Figure adapted from Dybeck et al.¹¹².

event that has been executed at least n_e times, is slowed down by a factor¹¹²:

$$\alpha_m = \min \left\{ 2N_f \frac{R_s}{r_m + r_{-m}}, 1 \right\}, \quad (3.17)$$

where N_f is a parameter that separates fast and slow reactions, and $-m$ means the reverse of step m . Thus, the fastest reactions are slowed down first and the most. As the algorithm proceeds, R_s approaches the escape-rate of the entire superbasis, and a non-equilibrated event will be executed. After firing a rare non-equilibrated event, all events are unscaled and the procedure is repeated. In this manner, the scheme solves the difficult time-scale separation issue of kMC.

In the introduction of the generalized temporal acceleration scheme¹¹², Fischer-Tropsch synthesis was modeled with Eley-Rideal steps, disregarding adsorbate-adsorbate interactions and adsorbate diffusion. This means that most non-equilibrated reactions are executable directly from all configurations in the superbasis, which is generally not the case. As an example, consider the surface reaction $A^* + B^* \rightarrow AB^* + *$ where A and B interact repulsively. Here, on average several quasi-equilibrated diffusion steps will proceed before the reactants become neighbors and the reaction is possible. Thereby, R_s is underestimated and the time-step of diffusion becomes unreasonably high; up to multiple seconds. To resolve this, it can be beneficial to set R_s equal the rate-constant of the fastest non-equilibrated reaction channel. This makes the algorithm escape the superbasis more conservatively, with an upper bound on the time-step. In this thesis, the generalized temporal acceleration scheme was implemented in MonteCoffee, as presented in **Paper III**. In MonteCoffee, it is also possible use the simple method of raising barriers for the fast steps with a constant value.

3.4 Analyzing Reaction Kinetics

One motivation to perform kinetic simulations is that data is generated that can be compared with experimental measurements. This section discusses the information that can be obtained in kinetic simulations, and how to analyze the results in relation to experiments.

3.4.1 Reaction Mechanisms

One advantage of a microkinetic analysis is that it provides information about the governing reaction mechanisms; provided that the relevant pathways are included in the simulations. The active mechanisms are found using the net-rates, which can be written in a mean-field picture as:

$$W_i = k_i^+ \prod_l \theta_l - k_i^- \prod_m \theta_m. \quad (3.18)$$

Where l is the set of reactant species for the elementary reaction i , and m is the set of products. In kinetic Monte Carlo, the net-rates are given by the number of executions over time. The dominant reaction mechanism will be the set of reactions with the highest net-rates that complete a catalytic cycle.

3.4.2 Turnover Frequencies and Coverages

The Turnover Frequency (TOF) reflects the number of products formed per active site and time-unit. In a kinetic model, the TOF can be extracted as the net-rate of product formation. Quantitative comparison between simulated TOFs and experimental results is generally complicated, since there are many uncertainties and approximations involved in the modeling. Hence, it not unusual that the simulated TOF deviates with some orders of magnitudes from experiments. However, the trends and variations across various reaction conditions often resemble experimental behavior.

Adsorbate coverages are simple measures to analyze reactions. The most abundant surface species can be compared to spectroscopic experiments, revealing the adsorbates on the surface. Knowing the most abundant species can improve modeling, for example by targeted refinement of adsorbate-adsorbate interactions or entropy estimates.

3.4.3 Reaction Orders and Apparent Activation Energies

The reaction order and the apparent activation energy are two macroscopic quantities that can be extracted from microkinetic models and compared with experimental data. The reaction orders and apparent activation energies are typically found by fitting Arrhenius-type power-laws of the rate against temperature and pressures:² (pp. 26-27,36-37):

$$r = A \exp\left(\frac{-E_{\text{app}}}{k_B T}\right) \prod_x p_x^{n_x}, \quad (3.19)$$

where, A is the pre-exponential factor, E_{app} is the apparent activation energy, p_x is the partial pressure in species x , and n_x is the reaction order in gas-species x . To obtain n_x from simulations, the TOF can be fitted to this power-law. In practice, E_{app} is calculated numerically by evaluating the derivative of r versus $1/T$, over a narrow temperature range.

Direct comparison with experimental data is not always possible as the surface structure in experiments is less well-defined than in theoretical models. For the methane oxidation reaction modeled in **Paper IV**, the reaction orders agreed with experiments^{116;117}. However, the apparent activation energy did not agree well with experimental values^{116–118}. This is likely due to surface oxidation during the experiments, which was not included in the model. In this manner, discrepancies between experiments and a validated microkinetic model can provide important insights about the catalyst state during experiments.

3.4.4 Degree of Rate Control

The degree of rate control^{119;120} of an elementary step (χ_i) reflects the sensitivity of the catalytic rate r to the individual rate constants. χ_i is defined by:

$$\chi_i = \frac{k_i^f}{r} \left(\frac{\partial r}{\partial k_i^f} \right)_{K_i}, \quad (3.20)$$

where k_i^f is the forward rate constant of step i , and the derivative is taken with a fixed equilibrium constant K_i . Thus, χ reveals the slow steps that limit the catalytic rate. The derivative can be evaluated numerically using finite differences, by increasing the rate constant of the step slightly ($\sim 1\%$). χ is important in microkinetic modeling as it determines the elementary steps that affect the rate. Therefore, χ can provide useful information for catalyst design. For single branch reaction mechanisms, it can be shown that $\sum_i \chi_i = 1$. Thus, χ_i reflects the relative importance of step i for the overall kinetics.

Paper V connects the microscopic kinetics to the reaction orders and apparent activation energies using the degree of rate control. In this way, these two macroscopic quantities are linked to the atomic understanding; a link that previously has been unclear for multi-step catalytic reactions¹²¹. We showed that the reaction orders have a simple relation to χ :

$$n_x = \sum_i \chi_i \frac{\partial \ln W_i}{\partial \ln p_x}. \quad (3.21)$$

Thus, the reaction order is a weighted sum over the individual rates W_i , differentiated with respect to the pressure of interest.

The relation between χ and the apparent activation energy was shown to be:

$$E_{\text{app}} = \sum_{i \in \text{vib}} \chi_i \left(E_i + k_B T + T^2 \frac{\partial S_i}{\partial T} \right) + \sum_{j \in \text{trans}} \chi_j \left(E_j - \frac{k_B T}{2} + k_B T^2 \frac{\partial P_j}{\partial T} \right) \quad (3.22)$$

$$- k_B T^2 \sum_x \frac{\partial n_x}{\partial T} \ln p_x,$$

where E_i is the energy barrier of elementary step i , S_i is the entropic barrier, and P_j is the sticking coefficient related to step j . The first sum runs over the steps with vibrational reaction coordinates, and the second sum over reactions having translational reaction coordinates. The third sum accounts for the pressure dependence of the total rate. The zeroth order term in temperature is the largest contribution, which arises from the elementary energy barriers. The first-order temperature terms arise from a lost degree of freedom in the reaction coordinate, and the second order terms stem from entropic losses and pressure dependencies.

The derived expressions provide a microscopic understanding of the reaction orders and apparent activation energies. The expressions might be used to evaluate proposed rate-determining steps and reaction mechanisms, for example by combining DFT calculations and experimental measurements. Thus, the apparent activation energy does not only reflect the bare energy barrier of the slowest elementary step. Previously, the reaction order in the presence of a catalyst has been described as a phenomenological quantity¹²¹. The derived expression (3.21) demonstrates the connection between reaction orders and the elementary reactions.

3.5 Practical Formulation of Kinetic Models

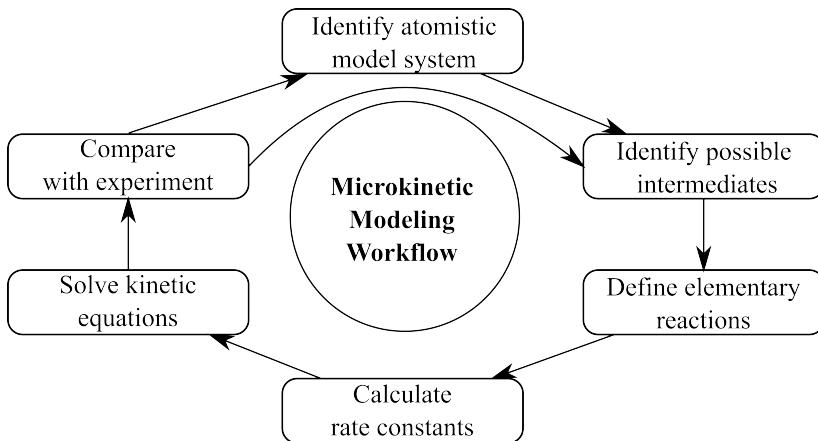
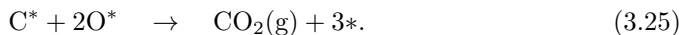
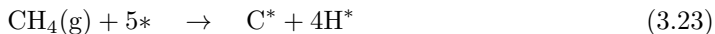


Figure 3.5: Illustration of workflow for constructing first-principles microkinetic models.

The models in this thesis were constructed using a workflow illustrated in Figure 3.5. Formulation and refinement of a model is an iterative procedure, where the cycle in Figure 3.5 is completed multiple times before settling on a final version of the kinetic model. The cycle begins with identifying an atomic model system of the catalyst. This is often a crucial and difficult step as technical catalysts are complex systems, which are ill-defined with respect to structure and composition. The next step is to identify intermediates, which are connected by multiple elementary reaction steps that define the catalytic cycle. Taking complete methane oxidation to CO_2 over Pd surfaces as an example, the atomic

model system can be Pd(100) or Pd(111). Plausible intermediates are hydrocarbons, oxygen, carbon, and CO. Thereby, a starting point for a possible reaction mechanism could be:

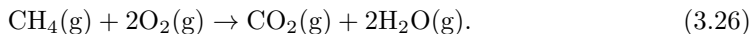


These steps should be reformulated as elementary steps, possibly by including alternative pathways. After the intermediates and elementary reactions have been identified, rate constants are calculated for the considered elementary steps and the kinetic equations are solved. Thereafter, the computational results are compared to experimental data by simulating measurable quantities, such as turnover frequencies, reaction orders, and apparent activation energies. The cycle is repeated until the model has the desired level of detail and agrees with experimental data. A validated microkinetic model opens up for the possibility to use the simulations for predictions beyond the experimentally investigated conditions.

3.6 Example: Analysis of Complete Methane Oxidation

When a microkinetic model has been formulated, computer simulations can be performed. Computer simulations have the advantage that they are relatively cheap, can show long-time behavior, and that causal connections can be addressed. In this section, a mean-field model of complete methane oxidation (**Paper IV**), is discussed to give an overview of what kind of information that can be obtained from a microkinetic model. KMC simulations can provide the same information, however requiring more extensive data-analysis.

In **Paper IV**, complete methane oxidation is modeled over Pd(100) and Pd(111). The reaction is crucial as methane is a potent greenhouse gas^{122;123}. Moreover, complete methane oxidation to CO₂ is becoming increasingly important for the automotive industry as the global natural-gas vehicle fleet grows¹²⁴. The overall reaction is:



Pt and Pd are known to be active catalysts, where Pt is superior in net reducing conditions and Pd is advantageous in net oxidizing environments¹²⁵. Pd oxidizes readily at most reaction conditions^{123;126–128}, and the high activity has been attributed to the oxidized phase in some cases^{126;129}, whereas other reports assigned the high activity to the metallic state^{130–132}. The metallic phase is difficult to stabilize during experiments, which makes a first-principles microkinetic model a useful tool to explore the kinetics.

The developed kinetic model extends a previous model of the reaction over metallic Pd⁵⁰ by including a larger number of reaction barriers and multiple reaction mechanisms. Furthermore, the model is constructed to compare with a previous detailed model of the reaction over PdO(101)⁴⁹. The model includes six gas-phase species, 16 adsorbed species, and 32 elementary reactions, which enables multiple reaction pathways. The included gas-phase species are: CH₄, O₂, CO₂, H₂O, CO, and H₂. Included adsorbates

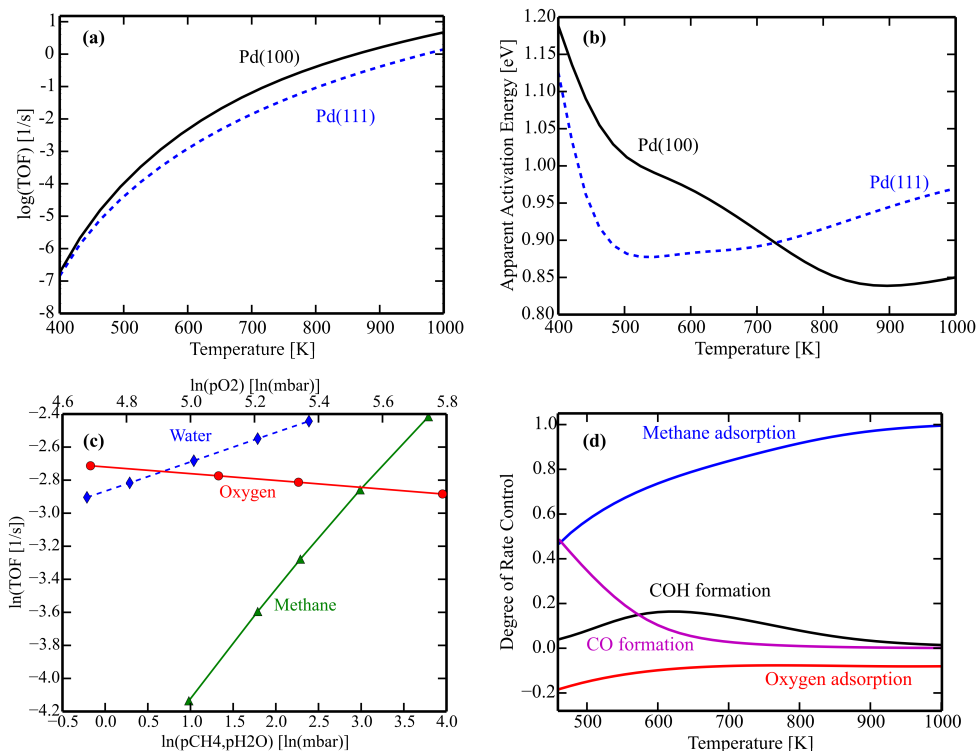


Figure 3.6: Simulated kinetics of methane oxidation at 0.61 mbar methane and 3.06 mbar oxygen. (a) Turnover frequencies versus temperature. (b) Apparent activation energies versus temperature. (c) Turnover frequency versus pressures on Pd(100) at 598 K. (d) Degree of rate control versus temperature on Pd(100).

are: CH_3 , CH_2 , CH , C , H , O_2 , O , CO , OH , H_2O , CH_2OH , CH_2O , CHO , COH , OCOH , and CHOH . The simulations were performed in slight oxygen excess with pressures of 0.61 mbar methane and 3.06 mbar oxygen.

The rates of the steady-state elementary steps revealed the dominant reaction pathway. At high temperatures, methane is sequentially dehydrogenated to $\text{C} + 4\text{H}$. Thereafter, C is oxidized to CO and further to CO_2 by O . Simultaneously, H is oxidized to H_2O , mainly via $\text{OH} + \text{OH} \rightarrow \text{H}_2\text{O} + \text{O}$. At lower temperatures, instead C is oxidized by OH , and the mechanism involves steps such as $\text{C} + \text{OH} \rightarrow \text{COH}$ and $\text{COH} + \text{O} \rightarrow \text{OCOH}$.

Coverages and TOFs can be obtained from microkinetic models. We found the most abundant adsorbates on the surfaces to be O , C and CO . O was present at all investigated temperatures on both Pd(100) and Pd(111), whereas C and CO only were present at low temperatures. The simulated TOFs are shown in Figure 3.6 (a). The TOFs vary seven orders of magnitudes when increasing the temperature from 400 to 1000 K, and the Pd(100) surface is more active than Pd(111) at all investigated conditions.

The apparent activation energy (E_{app}) partly reflects the Gibbs free energy barriers of the rate controlling steps, as was derived in **Paper V**. The simulated E_{app} is shown in

Figure 3.6 (b). E_{app} varies between 1.2 and 0.85 eV for Pd(100) in the temperature range 400-1000 K. The variation is due to changing reaction mechanisms and rate-controlling steps. In the limit of high temperatures, E_{app} is determined by the methane adsorption barrier and the oxygen adsorption/desorption equilibrium as:

$$E_{\text{app}} \approx E_{\text{CH}_4}^f - \frac{\sqrt{p_{\text{O}_2} K_{\text{O}_2} \Delta E_{\text{O}_2}}}{1 + \sqrt{p_{\text{O}_2} K_{\text{O}_2}}}, \quad (3.27)$$

where $E_{\text{CH}_4}^f$ is the energy barrier for dissociative methane adsorption, p_{O_2} is the oxygen pressure, ΔE_{O_2} is the dissociative adsorption energy of O_2 , and K_{O_2} is the equilibrium constant for oxygen adsorption.

The reaction orders reflects how the TOF responds to pressure changes. Figure 3.6 (c) shows the logarithm of the TOF as a function of methane, oxygen, and water pressure on Pd(100). The results for Pd(111) are similar. A higher methane pressure increases the TOF, and methane yields a reaction order close to 1. Conversely, oxygen inhibits the rate by blocking sites for methane dissociation and has a negative reaction order. At low temperatures, water can promote the reaction by increasing the rate of $\text{C} + \text{OH} \rightarrow \text{COH}$, which is a rate-controlling step.

The degree of rate control reflects the steps that determine the rate, and it explains the kinetics in a compact manner. Figure 3.6 (d) shows the simulated degree of rate controls for the main steps. The rate-controlling steps at low temperatures were found to be $\text{C} + \text{OH} \rightarrow \text{COH}$ and $\text{C} + \text{O} \rightarrow \text{CO}$. At higher temperatures, dissociative methane adsorption eventually becomes the rate-determining step. Oxygen adsorption is slightly inhibiting over the entire temperature range. These observations are reflected in the coverages, as the most abundant species are connected to the rate-controlling steps. C is present on the surface, which suggests that oxidizing C has a finite rate-control, in agreement with the analysis. The reaction orders are also explained by the degree of rate control, as is derived analytically in **Paper V**. The reaction order in methane follows the degree of rate control for methane dissociation closely (**Paper IV** and **Paper V**). The slightly negative oxygen order shows that oxygen adsorption is an inhibition step, and thus it has a negative rate control. The positive order in the water pressure is readily understood by noting that increasing the OH concentration speeds up the rate-controlling step: $\text{C} + \text{OH} \rightarrow \text{COH}$. The apparent activation energy is also connected to the degree of rate control (**Paper V**). The high-temperature analytical expression for the apparent activation energy (3.27), shows that methane adsorption is the most rate-controlling step, and oxygen adsorption is a slightly inhibiting step.

The model in **Paper IV** for metallic Pd can be compared with methane oxidation over PdO(101), which was modeled in detail previously⁴⁹. The reaction orders in the methane pressure are high and positive for both PdO^{49;116–118} and metallic Pd surfaces. However, the PdO catalyst has qualitatively different reaction orders in the water and oxygen pressures. Water is known to be poisoning the PdO catalyst^{49;116–118;133} due to site-blocking effects, whereas water can promote the reaction on metallic Pd. Oxygen can promote the reaction on PdO at some conditions^{49;117;118}, whereas it inhibits the reaction on metallic Pd. These clear qualitative differences between Pd and PdO can aid characterization of the active phase using only the reaction kinetics.

These results apply mainly to extended surfaces, however, technical catalysts are nanostructured materials. The presence of low-coordinated sites on nanoparticles could promote this reaction^{23;26} as methane adsorption is the rate-determining step.

Summary

The present chapter has discussed how the chemical master equation describes reaction kinetics. The mean-field approximation was discussed as an approximate solution to the master equation, and kinetic Monte Carlo was presented as a stochastic method to solve the master equation. Analysis of the results from microkinetic models was discussed with focus on comparing with experiments. Finally, the workflow in modeling was presented, and the information that microkinetic models can provide was discussed.

Chapter 4

Reactions on Nanoparticles

Heterogeneous catalysts are fabricated as metal nanoparticles (< 5 nm) supported on oxide surfaces, making it desirable to study the kinetics over nanoparticles. However, this is challenging as the mean-field approximation breaks down for finite-sized systems with multiple different sites, where kinetic Monte Carlo simulations are required. The present chapter presents and discusses results from kinetic Monte Carlo simulations of reactions over nanoparticles, which highlights the fundamental differences in reaction kinetics between nanoparticles and extended surfaces. The effects of particle size, shape, alloying, and strain are investigated. It is common to describe reaction kinetics of nanoparticles using the energetics of isolated sites²¹, which neglects long-range kinetic couplings. This might be appropriate for initial screening studies, however, herein it is shown that kinetic couplings are crucial to understand the kinetics of reactions over nanoparticles.

Paper VI- Paper IX investigate CO oxidation over Pt nanoparticles and Pt(111), which is an important reaction in automotive exhaust aftertreatment. The reaction is often applied as a model reaction, owing to its apparent simplicity and large pool of experimental data¹³⁴. The reaction was modeled using a simple Langmuir-Hinshelwood mechanism. We found that the facets enable O₂ dissociation, whereas the edges catalyze the CO₂ formation step. This bifunctional mechanism makes nanoparticles efficient as compared to extended surfaces.

Paper X explores hydrogenation of acetylene-ethylene gas mixtures, which is a central reaction in polymer chemistry. The reaction was modeled over Pd/Cu Single-Atom Alloy (SAA) nanoparticles, Pd/Cu(111), and Pd(111). Pd/Cu SAAs contain a minute concentration of isolated Pd atoms, embedded in Cu surfaces. This catalyst design can lead to a high selectivity^{135;136}. The Horiuti-Polanyi mechanism was used as a model mechanism, where acetylene is hydrogenated sequentially from C₂H₂ to C₂H₄. Desorption of C₂H₄ competes with overhydrogenation of C₂H₄ to undesired C₂H₆. Here, SAAs were found to enhance the selectivity as compared to pure Pd. Moreover, the selectivity of nanoparticles was found to be lowered due to edge and corner sites. The reaction mechanism over nanoparticles was found to be complex due to kinetic couplings. Thus, acetylene hydrogenation is affected by the Pd site placement, and likely also particle geometry.

4.1 Energy Landscape Representation

The reaction energy landscape is one of the most critical factors in reaction kinetics. The energy landscape for extended surfaces is, in principle, straightforward to map out using DFT calculations. However, the reaction energy landscape on nanoparticles is more complex^{23;24;26;137} as nanoparticles contain multiple different types of sites, demanding a

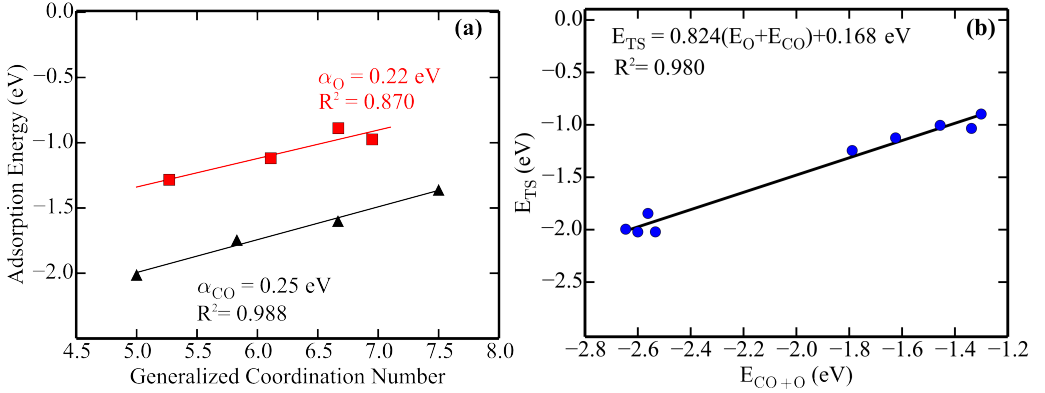


Figure 4.1: (a) The adsorption energies of CO (black) and O (red) over Pt as a function of $\overline{\text{CN}}$. (b) Calculated BEP relation for $\text{CO} + \text{O} \rightarrow \text{CO}_2(\text{g})$.

large number of energy calculations. Previously, simplified reaction energy landscapes^{52;54} and schematic reactions^{58;59} have been used to perform kMC simulations of reactions over nanoparticles. However, seemingly no studies have simulated specific reactions using detailed reaction energy landscapes over nanoparticles. In this thesis, the challenge of mapping out the nanoparticle reaction energy landscape was solved using scaling relations. This procedure captures the main features of a nanoparticle, namely, the energy differences between inner facet sites and low-coordinated sites. To reduce the computational cost further, Brønsted-Evans-Polanyi (BEP) relations were used to scale the reaction energy barriers. BEP relations have the advantage that adsorbate-adsorbate interactions easily can be included. Different descriptors, can be used to represent the reaction energy landscape, including the d-band center³⁴, coordination numbers^{138–140}, generalized coordination numbers^{141–143}, and the metal-site stability¹⁴⁴.

For CO oxidation on Pt nanoparticles, we described the reaction energy landscape using generalized coordination numbers. Recently, the generalized coordination number $\overline{\text{CN}}$ was shown to be a good descriptor for adsorption energies on nanoparticles and surfaces^{141–143}. $\overline{\text{CN}}$ is an extension of the conventional coordination number, which accounts for the coordination numbers of the nearest neighbors as:

$$\overline{\text{CN}} = \sum_{i \in \{NN\}} \frac{\text{CN}_i}{\text{CN}_{\text{max}}}, \quad (4.1)$$

where the sum runs over the nearest neighbors to the site in question, CN_i is the conventional coordination number of the nearest neighbor i , and CN_{max} is the maximally possible coordination number of neighbors in the bulk. In a fcc crystal, the ontop site has $\text{CN}_{\text{max}} = 12$, a bridge has $\text{CN}_{\text{max}} = 18$, a three-fold hollow has $\text{CN}_{\text{max}} = 22$, and for a four-fold hollow site $\text{CN}_{\text{max}} = 26$. It can be important to use $\overline{\text{CN}}$ as opposed to the conventional coordination number, since $\overline{\text{CN}}$ changes more smoothly between high and low-coordinated sites. In contrast, the conventional coordination number changes abruptly between a facet and edge. The smoothness in $\overline{\text{CN}}$ helps the adsorbates diffuse

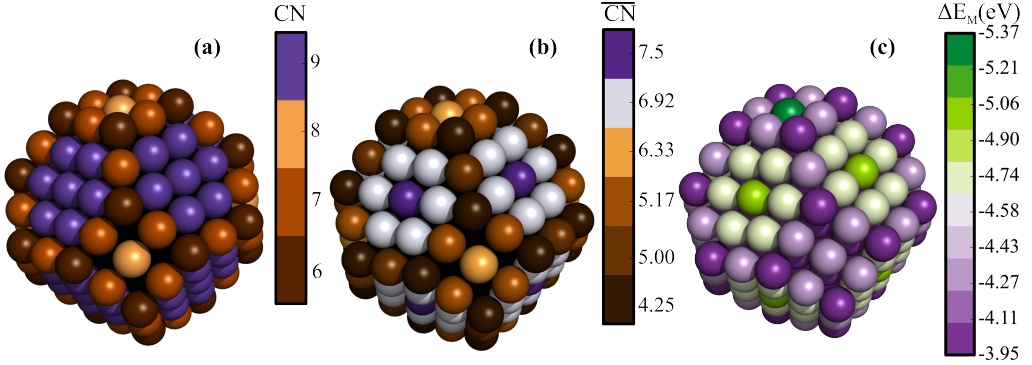


Figure 4.2: Energy landscape descriptors plotted for the 1.6 nm octahedron of **Paper X** with the Pd atom in the middle of the top (100) facet. (a) Conventional coordination number, (b) generalized coordination numbers of ontop sites, and (c) metal-site stability of ontop sites.

towards certain low energy positions. Figure 4.1 illustrates how $\overline{\text{CN}}$ is used to represent the reaction energies over nanoparticles. The adsorption energies of CO and O are functions of $\overline{\text{CN}}$, and the energy barrier is a function of the adsorption energies. Thus, $\overline{\text{CN}}$ determines the entire reaction energy landscape.

For alloys, $\overline{\text{CN}}$ cannot directly be used as a descriptor as it contains no information about which element that defines the sites. Thus, to describe the Pd/Cu nanoparticles in acetylene hydrogenation, the metal-site stability¹⁴⁴ (ΔE_M) was used as a descriptor for the energies. ΔE_M implicitly contains information about alloying effects. ΔE_M for a site reflects the site's binding-strength in the nanoparticle, which can be calculated as¹⁴⁴:

$$\Delta E_M = E_{M-S} - E_M - E_S(g) \quad (4.2)$$

where E_{M-S} is the metal's energy including the site, E_M is the energy of the metal with the site removed, and $E_S(g)$ is the energy of the site in a large calculation cell. To fit the most accurate scaling relation for a specific adsorbate, E_{M-S} was calculated from a relaxed structure including the adsorbate. From this relaxed structure, E_M and $E_S(g)$ were derived from single point energy calculations. Using ΔE_M requires a slightly higher number of calculations as compared to $\overline{\text{CN}}$, as ΔE_M is not a purely geometric quantity.

It is instructive to compare the different descriptors for the reaction energy landscapes. Figure 4.2 illustrates the conventional coordination number (CN), $\overline{\text{CN}}$, and ΔE_M for the ontop sites of the 1.6 nm Pd/Cu single atom alloy nanoparticle, used to model acetylene hydrogenation. CN and $\overline{\text{CN}}$ seem equally good at describing (111) sites that are surrounded by identical (111) sites. However, CN does not capture the sequential drop in coordination when moving from the inner (111) facet towards the edges. Similarly, $\overline{\text{CN}}$ is highly correlated with ΔE_M , however, the Pd site in the Cu nanoparticle has a very different reactivity, which CN and $\overline{\text{CN}}$ do not directly capture. Despite of this, it may be possible to use $\overline{\text{CN}}$ to fit separate scaling relations for the alloy and mono-metallic sites.

4.2 Reaction Mechanisms

Nanoparticles contain a range of different sites, which results in more complex reaction mechanisms as compared to extended surfaces. The main steady-state reaction mechanism follows the principle of least resistance¹⁴⁵, where the reactions proceed through the lowest energy pathway. Thus, the elementary steps can preferentially proceed over specific sites. The principle of least resistance and multiple sites on nanoparticles make reaction mechanisms a non-intuitive subject.

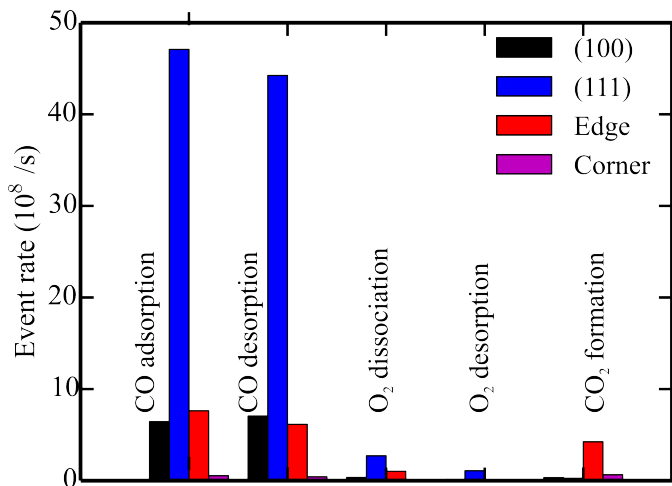


Figure 4.3: Steady-state rates of elementary steps in CO oxidation on a 5.2 nm truncated octahedron Pt particle. Temperature: 1100 K, pressures: CO 20 mbar, O₂ 10 mbar.

The mechanism for CO oxidation over Pt nanoparticles was found to follow a reaction pathway governed by kinetic couplings between multiple sites. Figure 4.3 shows the rates for the elementary steps of the different sites on a 5.2 nm truncated octahedron. CO adsorption and desorption are nearly equilibrated on the facets. O₂ dissociation proceeds preferentially over the (111) facets, as it requires two free sites and the (111) facet has the most free sites. Moreover, O₂ dissociation is slightly out of equilibrium on the (111) facets. CO₂ formation proceeds mainly over edges. This shows a reaction mechanism where diffusion steers CO and O towards the edges where CO₂ is formed. Thus, kinetic couplings between facets and edges are crucial to understand reactions over nanoparticles. Extended surfaces contain only one type of site, and are therefore not able to split up the reaction mechanism over different types of sites, in this bifunctional manner.

To investigate the kinetic couplings in CO oxidation, we disabled different parts of the particle to investigate the response of the remaining sites. In this manner, the difference can be discovered between the sites in the system and sites in isolation. Figure 4.4 shows a kMC simulation of the TOF for various pairs of nanoparticle-sites. The figure compares a full simulation to a simulation, where all (111) sites are disabled. Naturally, the edge-(111) reaction channel was killed when the (111) sites were disabled. However, the edge-edge

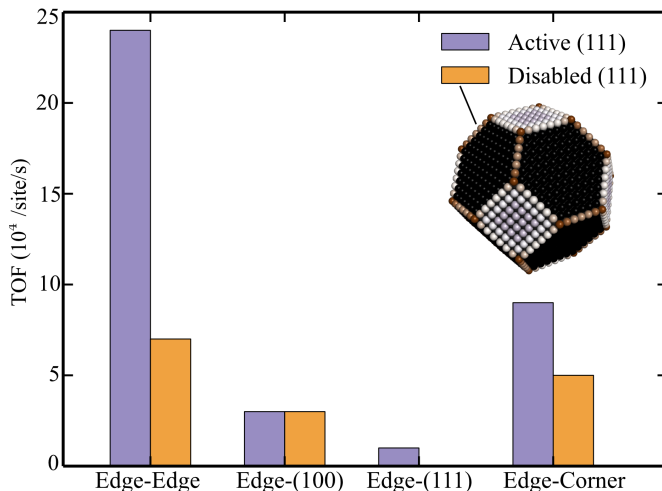


Figure 4.4: CO oxidation turnover frequency of a 5.2 nm truncated octahedron. TOF is deconvoluted into different reaction channels for a regular simulation (orange) and all (111) sites disabled (purple). Temperature: 1100 K, pressures: $p_{\text{CO}} = 20$ mbar, $p_{\text{O}_2} = 10$ mbar.

and edge-corner TOFs also depended significantly on (111) sites. This non-linear behavior shows that long-range couplings are indeed important to understand the reaction over nanoparticles. Kinetic couplings can be important for a large range of particle sizes, since adsorbate diffusion often is facile. For example, the CO diffusion barrier on Pt(111) is about 0.06 eV, which at a typical reaction temperature of 600 K amounts to a diffusion rate of 4×10^{12} sites \cdot s⁻¹. An octahedral nanoparticle of 2.8 nm in diameter contains about 400 surface ontop-sites, and the molecule can circle an empty particle billions of times per second.

The reaction mechanism of acetylene hydrogenation over Pd/Cu single-atom alloys was also found to be strongly affected by kinetic couplings. Figure 4.5 (a) shows the rate of ethane formation [$\text{C}_2\text{H}_5^* + \text{H}^* \rightarrow \text{C}_2\text{H}_6(\text{g})$] for the Pd and Cu sites on the extended Pd/Cu(111) surface and sites on a Pd/Cu nanoparticle. For the extended Pd/Cu(111) surface, the Cu sites are the main sites where C_2H_6 is formed. In contrast, for the nanoparticle, the Pd site yields a two orders of magnitudes higher C_2H_6 rate than Cu. This is surprising as the reaction energies are identical on the Pd sites in Pd/Cu(111) and the nanoparticle. The Cu sites of the inner (111) and outer (111) facets have different C_2H_6 rates, which partly is attributed to the finite size of the facet. The (100) facets, edges, and corners show a lower activity than the outer (111) sites. However, on the edges and corners, ethylene hydrogenation [$\text{C}_2\text{H}_4^* + \text{H}^* \rightarrow \text{C}_2\text{H}_5^*$] is fast relative to ethylene desorption, which lowers the selectivity.

The reaction rates were found to be different at different areas of the particle. Figure 4.5 (b) shows the C_2H_6 production as a colormap. The sites closest to the Pd site are most affected by the alloying, and produce the most C_2H_6 . Multiple Pd site placements were tested, and it was found that the location of the Pd site has a significant effect on the

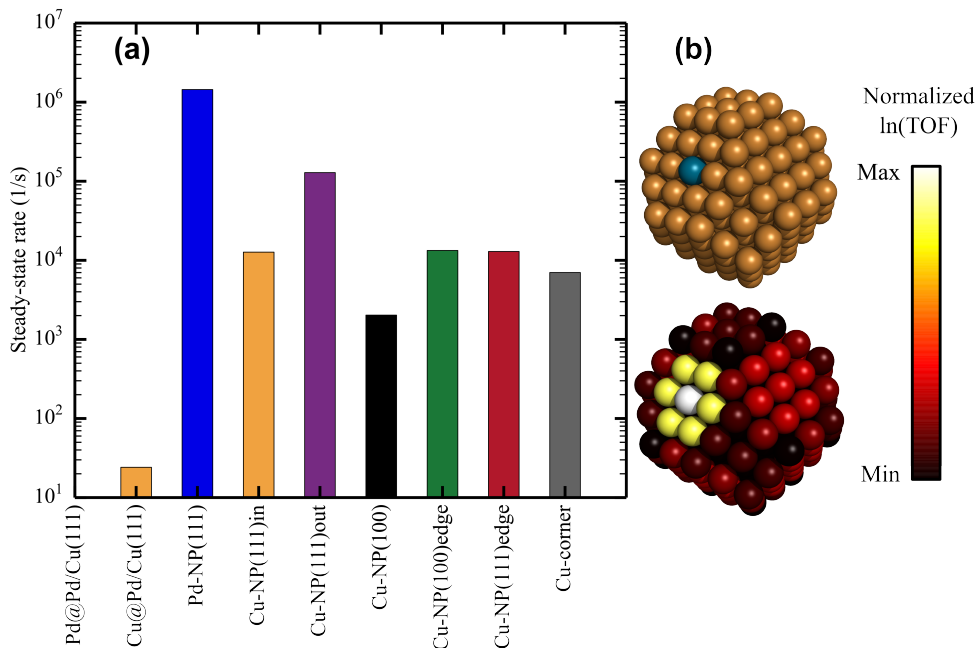


Figure 4.5: (a) C_2H_6 net-rate for the Pd and Cu sites on Pd/Cu(111), and 1.6 nm Pd/Cu truncated octahedron with one Pd atom in a (111) facet. (b) particle geometry (Pd=blue, Cu=brown) and normalized logarithmic C_2H_6 TOF as a colormap. Temperature: 320 K, pressures: $p_{C_2H_2} = 1$ mbar, $p_{C_2H_4} = 10$ mbar, $p_{H_2} = 10$ mbar.

selectivity. However, no obvious relation between the Pd/Cu alloying energy and selectivity was found. Comparing nanoparticles to extended Pd/Cu(111), the nanoparticles contain multiple different sites, which couple kinetically. For Pd/Cu(111), the Pd and Cu sites also couple, however, to a much lesser extent. Moreover, the rates on the nanoparticle were found higher than on Pd/Cu(111), and the selectivity was lower.

Both in CO oxidation and acetylene hydrogenation, the TOFs are increased by the presence of multiple types of sites on the nanoparticles. Kinetic couplings can make two identical sites yield different rates; if one site is placed inside a finite facet and the other in an extended surface. Thus, a nanoparticle design strategy could be to combine sites that are optimized for each elementary step. However, this must be done in a manner where no sites will lower the selectivity. For CO oxidation, there should be a balance between edge sites and (111) facets. For acetylene hydrogenation, the Pd site, edges, and corners yield a lower selectivity, whereas (111) sites yield a high selectivity. Therefore, a design strategy for acetylene hydrogenation is to fabricate large icosahedral Cu nanoparticles with a low Pd concentration. The results show that the concept of an active site may be expanded to include distant sites in a site-assembly. For site-assemblies, the kinetic bottlenecks may not be well-described by the degree of rate control as this does not differentiate between site-types. Thus, to enable rate-control analysis over nanoparticles,

the degree of rate control can be redefined as a tensor $\chi_{ik\ell}$, which reflects the response of the TOF on site-type ℓ to a change in rate constant of step number i at site-type k . In this manner, understanding the reaction mechanisms for nanoparticles may help improve catalyst design by investigating the complex kinetic couplings.

4.3 Effects of Particle Morphology

Industrial catalysts contain a distribution of nanoparticles with various shapes and sizes¹⁴⁶, which can influence catalytic activity and selectivity significantly for some reactions^{147–153}. Moreover, dynamical changes in shapes have been observed experimentally¹⁴. Thus, it is relevant to investigate the effects of particle size and shape on catalytic activity. This problem has been addressed experimentally, and different reactions have been found to be sensitive to the particle shape^{147;152;153}. Theoretically, shape and size effects have usually been investigated by isolated nanoparticle sites^{45;138;139}, for example by calculating how the number of edge sites grow with particle diameter. However, kinetic couplings dominate reactions over nanoparticles, which implies that isolated sites cannot be used to derive size and shape effects.

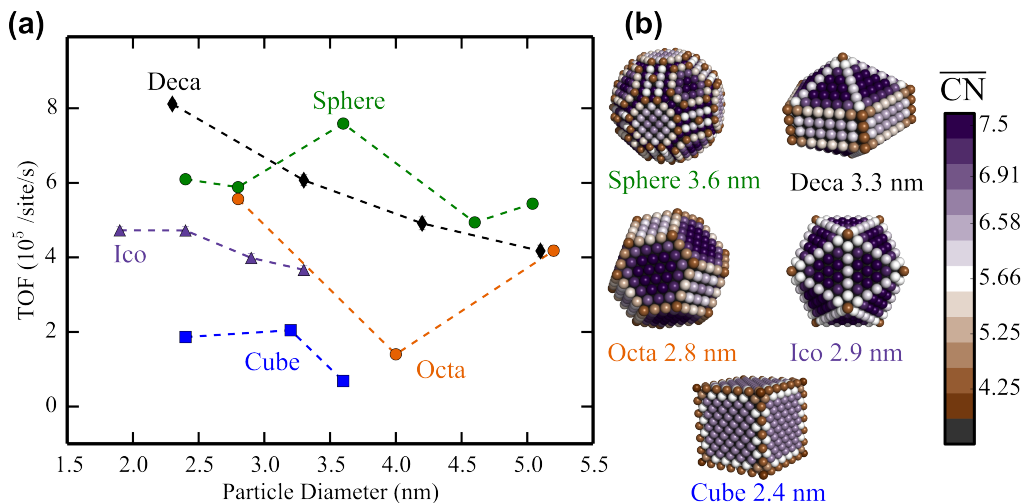


Figure 4.6: (a) CO oxidation TOF of the considered particle shapes and sizes. (b) Particle shapes at selected sizes and a colormap of \overline{CN} for the ontop sites. Temperature: 1100 K, pressures: $p_{CO} = 20$ mbar, $p_{O_2} = 10$ mbar.

The effect of particle size was investigated for CO oxidation over Pt in **Paper VI** and **Paper VII**. Particle size was shown to be important for truncated octahedrons, partly since the most active site changes with reaction conditions. At low pressures and high temperatures, the edges and corners were found most active, whereas at high pressures and low temperatures, the facets became most active. Thus, larger particles were found most efficient at high pressures as the facets are present in larger fractions. However, different particle shapes result in different relations between particle size and TOF. Figure

4.6 shows the TOF as a function of particle diameter for different particle shapes. For small diameters, the decahedral nanoparticles yield the highest TOF, whereas spheres are most active for larger particle sizes. The presented curves have different shapes. This is partly owing to how many sites of each type that is added when increasing the diameter. For example, when increasing the diameter of cubes, only (100) facets and edges are added, whereas spheres add multiple types of sites. The TOF for each type of site was found to depend strongly on the particle geometry, owing to kinetic couplings. Thus, only a weak correlation between the reaction energy of a site and its TOF was observed. Therefore, it is not only important which the types of sites that are present, but rather the total site-assembly should be considered.

CO oxidation was studied at elevated temperatures, however, the particles likely remain solid. The melting point of a Pt nanoparticle can be estimated from its average coordination number¹⁵⁴ using the melting point of bulk Pt, which is¹⁵⁵ 2033 K. A 3 nm truncated octahedral Pt nanoparticle with average CN = 10.48 has a predicted melting point of 1775 K.

For the acetylene hydrogenation reaction over Pd/Cu nanoparticles, the effects of shape and size were not directly simulated. However, kinetic couplings were observed, which shows that such geometric effects could be important.

These findings demonstrate that it is important to explicitly consider different particle shapes and sizes when modeling reaction kinetics; an often neglected component in computational catalysis. Furthermore, it is important to consider nanoparticles from a systemic point of view, as opposed to a set of isolated functioning sites. Thus, even if the energy barriers are lowest on the (111) facets, it does not necessarily imply that icosahedral nanoparticles are most efficient. For catalysts designed to operate over a large range of reaction conditions, it could be beneficial to fabricate a wider distribution of nanoparticle shapes and sizes.

4.4 The Strain-Activity Relation

Supported nanoparticles are known to be strained. The strain can be intrinsic in the particle, or be imposed from external sources that alter the chemical properties of the catalyst. Therefore, it is important to investigate relationships between strain and catalytic activity. When a transition metal is subject to strain, the d-band width changes, and to keep a constant degree of filling, the d-band center moves in energy^{34;156}. This changes the adsorption energies as the adsorbate-orbitals hybridize with the d-band. The effects of strain on reaction kinetics have previously studied for CO oxidation over Pt(111) using mean-field microkinetic modeling¹⁴⁸. However, the kinetics for nanoparticles have remained unexplored. In this thesis, the effect of strain in CO oxidation over Pt nanoparticles is investigated. The effect of strain was found to be determined by kinetic couplings. Thus, the influence of strain can depend strongly on the specific strain pattern, and thus, particle shape, size, and reaction conditions.

In **Paper VIII**, the effects of strain in CO oxidation are compared for Pt(111) and Pt nanoparticles using kMC simulations. For simplicity, only homogeneous full-particle strain was investigated. Figure 4.7 (a) shows the response of TOF to strain for a 3.5 nm truncated octahedral nanoparticle and Pt(111). Pt(111) responds to strain in a linear

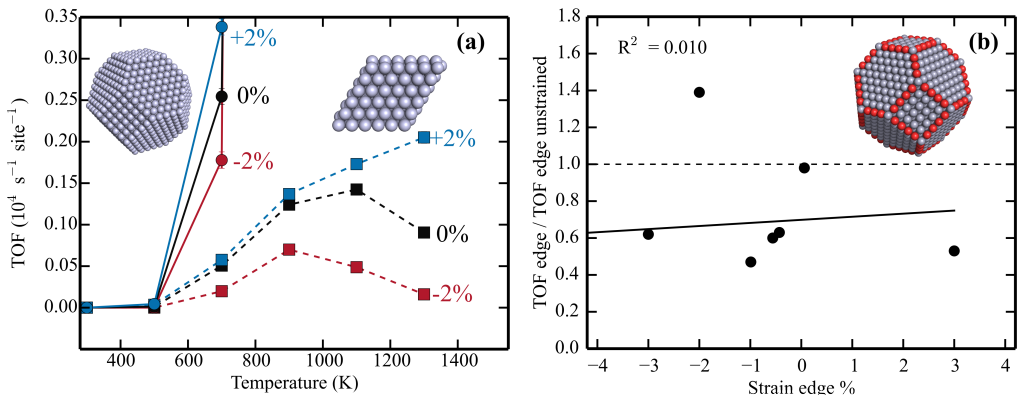


Figure 4.7: (a) The CO oxidation TOF as a function of temperature for a 3.5 nm truncated octahedral nanoparticle (dots) and Pt(111) (squares) for different strain values. (b) Average TOF of edges as a function of the average strain on edges at a temperature of 1100 K. The different points correspond to different strain patterns sampled from the TEM images of **Paper IX**. Pressures: $p_{\text{CO}} = 20 \text{ mbar}$, $p_{\text{O}_2} = 10 \text{ mbar}$.

fashion: Compressive strain decreases the TOF, whereas expansive strain increases the TOF. The decrease in TOF with compression comes the fact that both CO and O is bound weaker for compressive strain. For nanoparticles the same trend is seen to hold at low temperatures. However, in the limit of high temperatures where edges and corners become more active, the most beneficial strain-value changes significantly. Compared to Pt(111), the nanoparticle has a lower light off temperature, despite the higher average CO binding energies. This is a clear signal that kinetic couplings are present between the multiple sites of nanoparticles.

In **Paper IX**, the kMC simulations are performed using measurements of strain from Transmission Electron Microscopy (TEM) for supported Pt nanoparticles. The TEM images revealed that the particle-strain is sizable in magnitude (up to over 10%) and that many sites are subject to some degree of strain. The largest strains were located near the particle-support interface. Adding 5% of strain to the simulations changes the binding energy of CO and O by about 0.5 eV, which is a significant difference. However, when applying a large strain in the simulations, the catalytic activity responds by less than an order of magnitude. Thus, when some sites are strained, the reaction can find another pathway, in agreement with the principle of least resistance¹⁴⁵. This again highlights that kinetic couplings are important as nanoparticles respond non-linearly to strain. The response is particularly interesting for edge sites, which are the most active sites after light-off. Figure 4.7 (b) shows the average change in TOF of edges as a function of the average strain of the edges. Despite the edges being the most active site, there is little to no correlation between the edge-strain and the edge-TOF. This result is surprising as the reaction energy barrier for $\text{CO}^* + \text{O}^* \rightarrow \text{CO}_2(\text{g})$ is a linear function of strain.

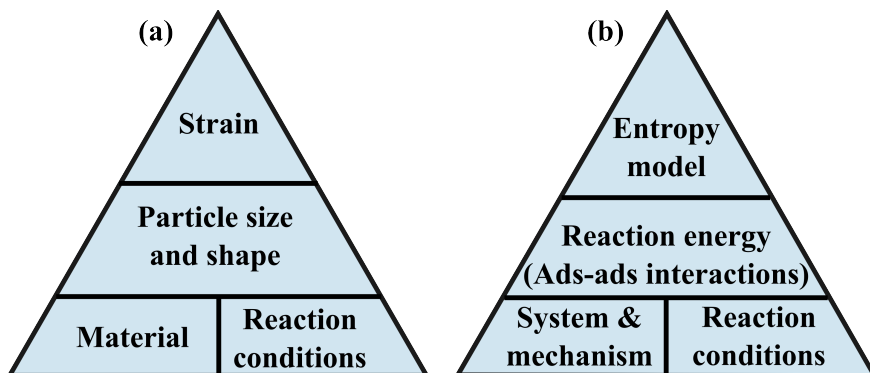


Figure 4.8: (a) Hierarchy of effects influencing reactions over nanoparticles. (b) Hierarchy of factors influencing kinetic modeling. The base of the pyramid is most important. The bottom levels influence the top levels.

4.5 A Hierarchy of Effects

The findings of this thesis illustrate that the turnover frequency of reactions over nanoparticles is determined by multiple factors. For a given reaction, these factors may include: catalyst material, support material, reaction conditions, particle size, particle shape, and strain. Whence, we can order these effects in a hierarchy of importance for computational modeling and catalyst design.

For catalyst design, the hierarchy could be represented by a pyramid as shown in Figure 4.8 (a). The most important design parameter is the catalyst material for a given set of reaction conditions. After the material and operating conditions are decided, particle size and shape become important to address. That is, the material and reaction conditions have a stronger effect on the catalytic reaction than particle size and shape, which can be inferred by comparing the results of **Paper VI-Paper IX**. The top of the pyramid is strain, which is likely the weakest of the effects investigated in this thesis. The optimal strain design likely depends strongly on the lower levels of the pyramid, such as material and reaction conditions.

The hierarchy of factors that influence kinetic modeling are illustrated in Figure 4.8 (b). The model system, considered reaction mechanisms, and the reaction conditions are foundational for modeling. For example, **Paper VI-Paper X** show that it is important to model nanoparticles explicitly to realize that edges and facets can operate in synergy to catalyze the reaction. If instead extended surfaces were modeled, this conclusion could not have been reached. The middle level of the pyramid is reaction energies and the related adsorbate-adsorbate interactions. The top level is the entropy modeling, which can have a weaker, yet appreciable, influence on the simulations. Entropy is placed in the top as the choice of entropy model depends on the reaction energies. These pyramids should be viewed more as guidelines than absolute statements, since the levels are not mutually exclusive, and may depend on other factors.

4.6 Methodological Considerations in Kinetic Modeling

Kinetics insights help understanding reaction mechanisms and performance bottlenecks in catalytic reactions. A common indirect method to understand kinetics is to analyze reaction energy landscapes using electronic structure calculations. This method may provide a crude picture of the kinetic behavior, however, more detailed kinetic simulations are often required. Kinetic simulations can be performed using a reductionist approach, where the reaction is simulated for isolated sites that represent the entire nanoparticle. This level of detail can provide crucial information about the kinetics for simple systems such as extended surfaces. However, to understand kinetics for nanoparticles, a systemic approach is required. A systemic approach combines different sites into a system that is treated as a whole entity. The kinetics of the system may be different than a linear addition of site-performances. This allows for a bottom-up understanding that ultimately may lead to more accurate screening studies. Thus, both systems theory and reductionist approaches are required to gain deep insights into catalysis.

Kinetic modeling involves a range of choices and approximations, including the model system, simulation method (kMC or MFA), reaction energy landscape, adsorbate-adsorbate interactions, and entropy modeling. In the present work, the model systems were chosen to be extended surfaces and idealized small nanoparticles. This enables a direct comparison between the two types of systems, and allows for investigating the materials gap. The overall conclusion is that the multiple sites on nanoparticles makes it preferable to model technical catalysts using nanoparticle systems. Whether the complexity of the model system needs to be increased further, for example by including oxide-supports, remains an open question.

The simulation methods chosen in this thesis were based on the fact that the mean-field approximation breaks down in the presence of multiple different sites and finite systems. Thus, the MFA was only applied in the studies that solely treated extended surfaces. KMC simulations are necessary to study nanoparticles, and to compare directly with extended surfaces, kMC was performed in the cases that treated both nanoparticles and extended surfaces. The simulations revealed that kMC simulations are extremely important to perform for nanoparticles, since kinetic couplings dominate the investigated hydrogenation and oxidation reactions. Thus, a simulation method that accounts for the specific geometric placement of sites is required.

The reaction energy landscapes can be calculated using different approaches. In the present work, DFT was used to obtain a balance between computational cost and accuracy. This balance is understood with respect to the fact that model systems are used as simulations cannot fully capture the complex technical catalysts. If technical catalysts were simulatable, likely the results would be too complex to analyze. In this respect, searching for chemical accuracy in modeling technical catalysts is likely futile. However, for more well-defined systems, it is sensible to strive for highly accurate energy calculations. Reaction energy landscapes can be computed directly or represented using descriptors. For extended surfaces, it is feasible to directly calculate the reaction energy landscape. However, nanoparticles contain multiple different sites placed in specific geometries, which requires several calculations. Thus, herein the reaction energy landscapes on nanoparticles were treated with descriptors, which is reasonable considering the uncertainties in the

DFT calculations. The uncertainty related applying fitted scaling relations is negligible, since the difference in adsorption energies between the nanoparticle-sites exceeds the uncertainty for the studied adsorbates. Adequate descriptors need to capture the main features of the nanoparticle energies. For example, for adsorbates to diffuse to the lowest energy sites, it is crucial to describe the sequential changes in energy between an inner (111) facet site and a corner site.

The kMC models of this thesis applied coarse-graining of the sites to entail ontop, bridge, and hollow binding positions. Hence, the most stable adsorbate binding position represents the entire coarse-grained cell. This method saves computational time, and is sensible if the rate constants do not depend on the detailed binding position. However, the implications of this approach should be further explored.

Adsorbate-adsorbate interactions were calculated on the extended surfaces. For the MFA models, the adsorbate-adsorbate interactions were implemented as functions of the coverages, and the kMC simulations include first-nearest neighbor pairwise interactions. Thus, the kMC simulations apply a somewhat simplified scheme, which captures the main contributions to the adsorbate-adsorbate interactions. However, the limitations of the present approach should be further explored as the adsorbate-adsorbate interactions can play a large role both for entropies and enthalpies. This could be achieved systematically using graph-theoretical methods and cluster expansion Hamiltonians^{111;157}.

Entropy modeling was investigated in the present work. It was found that direct potential energy sampling can improve kinetic modeling. Appropriate entropy modeling is particularly important at large temperatures since the Gibbs free energy depends linearly on TS . However, if entropy is to be described more accurately, it is important that the energy calculations are precise. For the CO oxidation reaction, the RPBE exchange-correlation functional yields good reaction energies as compared to experiments over Pt(111)⁶³. With such a well-defined system and accurate energies, it is sensible to improve the entropy description. For zeolites, it was shown that the entropy is about one order of magnitude larger than what was obtained with the harmonic approximation. Thus, in zeolites it is necessary model the entropy in greater detail.

Chapter 5

Conclusion & Outlook

With the present state of accuracy and speed of electronic structure calculations, it is relevant to formulate first-principles kinetic models. This thesis has investigated and developed the methodology of first-principle kinetic simulations of catalytic reactions over nanoparticles. This was realized in a series of papers that investigated central factors for the methods of microkinetic modeling. Electronic structure calculations were performed using density functional theory, and rate constants were modeled in transition state theory. Kinetic Monte Carlo simulations were deemed necessary to model nanoparticles, as the mean-field approximation breaks down for finite systems containing multiple different sites. The kinetic Monte Carlo simulations were realized by developing an open-source Python package named MonteCoffee.

Adsorbate entropy modeling was studied in the context of kinetic simulations. To enable systematic calculations of adsorbate entropy, a method named Complete Potential Energy Sampling (CPES) was developed. CPES was applied to model CO oxidation over Pt(111), where the method was shown to improve agreement with experiments as compared to the traditional harmonic approximation and free translator model. Moreover, CPES was applied to calculate molecular entropy in zeolite systems, where the molecular degrees of freedom are coupled due to interactions with the zeolite-framework. It was concluded that in zeolites, potential energy sampling is required to capture the nature of the molecular degrees of freedom.

Analysis of kinetic simulations was discussed in relation to experiments; exemplified using the developed microkinetic model of complete methane oxidation over Pd(100) and Pd(111). Experiments that address kinetics can reveal macroscopic quantities, such as reaction orders and apparent activation energies. Herein, the degree of rate control was used to link atomic understanding with macroscopic observables. An analytical expression was derived that relates the degree of rate control to the apparent activation energy and reaction orders.

Kinetic Monte Carlo simulations of reactions over nanoparticles have been challenging as calculations of the reaction energy landscape is computationally expensive. Herein, the reaction energy landscape was described using scaling relations in the generalized coordination number and metal-site stability. The energy barriers were scaled using Brønsted-Evans-Polanyi relations, and adsorbate-adsorbate interactions were included between first nearest neighbors. CO oxidation was simulated over Pt nanoparticles and Pt(111). Over nanoparticles, the reaction was found to be dominated by complex kinetic couplings between the multiple different sites, enabled by adsorbate diffusion. Thus, extended surfaces were found to be inadequate model systems for nanoparticles. The kinetic couplings were found to influence the relation between catalytic turnover frequency and particle shape, size, strain, and reaction conditions. In addition to CO oxidation,

selective hydrogenation of acetylene was modeled over Pd/Cu single-atom alloys. The reaction was compared for Pd(111), Pd/Cu(111), and Pd/Cu nanoparticles. Alloying Pd with Cu is found beneficial for selectivity, owing to modification of the relative energy levels. Over nanoparticles, the reaction mechanism was found to be complex and dominated by kinetic couplings between the sites. The edges and corners lower the selectivity, and the present reaction benefits from large icosahedral Cu particles, with a minimal Pd concentration. Hence, it is concluded that explicit kinetic simulations of nanoparticles are necessary to capture the complexity of heterogeneously catalyzed reactions. Moreover, nanoparticles must be understood from a systemic point of view and cannot be treated as a set of isolated sites.

To extend this thesis, there are multiple interesting aspects that can be investigated. For example, the method of modeling adsorbate-adsorbate interactions on nanoparticles can be studied in greater detail, both for adsorption energies and entropies. A limitation of the present work is that it treats the catalyst nanoparticle as a static entity without including morphological changes. Such dynamical changes could possibly be simulated by combining the developed Monte Carlo algorithm with molecular dynamics. Furthermore, an oxide-support may be included in the simulations to study possible spill-over phenomena.

As Richard Feynman envisioned it in his talk¹ almost 60 years ago, presently we have a much greater range of possibilities for manipulating and designing nanoscaled systems. When designing nanoscale technology, it is central to understand the quantum mechanical behavior of atomic systems, and the consequences this behavior has on macroscopic catalytic properties. This thesis has improved the understanding of heterogeneous catalysis, by developing the methodology for first-principles kinetics over nanoparticles.

Acknowledgments

The research was carried out at the Division of Chemical Physics and Competence Centre for Catalysis at Chalmers University of Technology, Göteborg, Sweden in the period August 2015 to March 2019.

The research is funded by Chalmers Excellence Initiative Nanoscience and Nanotechnology, the Competence Centre for Catalysis, and the Swedish Research Council. Computational time was granted by SNIC at C3SE (Göteborg) and PDC (Stockholm).

The Competence Centre for Catalysis is hosted by Chalmers University of Technology and financially supported by the Swedish Energy Agency and the member companies AB Volvo, ECAPS AB, Johnson Matthey AB, Preem AB, Scania CV AB, Umicore AG & Co. KG and Volvo Car Corporation AB.

In addition, I would like to acknowledge a non-exhaustive list of people:

My main supervisor, Henrik Grönbeck. Thank you for investing a lot of time and effort in supervising this project, and for our many scientific discussions. It has been very rewarding to learn from your analytical skills and scientific insights. I hope you will develop further on our findings, in the future.

My co-supervisor, Anders Hellman. You are acknowledged for serious as well as informal discussions, and for helping with both micro and macroscopic issues.

All my past and present colleagues at Chemical Physics are acknowledged. Thank you for creating a pleasant and nice working environment. I especially would like to thank Adam, Anna, Alvaro, Baochang, Chris, David, Lin, Lucy, Matthias, Maxime, Michael, Mikael, and Unni.

I would also like to acknowledge the members of the Competence Centre for Catalysis and co-workers at Chalmers. In particular I would like to thank Andy, Carl-Robert, David, Eva, Johan, Johanna, Peter, Simone, Ting, and Torben.

My extended family, and in particular Dorthe. You are acknowledged for extraordinary support. Without you this thesis would not have been possible.

Thank you all for entering the universal many-body wavefunction. No achievements should be viewed entirely in isolation.

Bibliography

- [1] Feynman, R. P. There's Plenty of Room at the Bottom. *J. Microelectromech. Syst.*, *1* (1992), 60–66. doi: 10.1109/84.128057.
- [2] Chorkendorff, I. and Niemantsverdriet, J. W. *Concepts of Modern Catalysis and Kinetics*. WILEY-VCH Verlag GmbH & Co. KGaA, Weinheim, second, revised and enlarged edition, 2007.
- [3] Robertson, A. J. B. The Early History of Catalysis. *Platinum Metals Rev.*, *19* (1975), 64–69.
- [4] Mars, P. and van Krevelen, D. W. Oxidations carried out by means of Vanadium Oxide Catalysts. *Chem. Eng. Sci.*, *3* (1954), 41–59. doi: 10.1016/S0009-2509(54)80005-4.
- [5] Taylor, H. S. A Theory of the Catalytic Surface. *Proc. R. Soc. Lond. A*, *108* (1925), 105–111. doi: 10.1098/rspa.1925.0061.
- [6] Eyring, H. The Activated Complex and the Absolute Rate of Chemical Reactions. *Chem. Rev.*, *17* (1935), 65–77. doi: 10.1021/cr60056a006.
- [7] Squires, G. Francis Aston and the Mass Spectrograph. *J. Chem. Soc., Dalton Trans.*, *0* (1998), 3893–3900. doi: 10.1039/A804629H.
- [8] Liljas, A. Background to the Nobel Prize to the Braggs. *Acta Cryst.*, *A69* (2013), 10–15. doi: 10.1107/S0108767312031133.
- [9] Duke, C. B. The Birth and Evolution of Surface Science: Child of the Union of Science and Technology. *PNAS*, *100* (2003), 3858–3864. doi: 10.1073/pnas.0730358100.
- [10] Österlund, L.; Grant, A. W.; and Kasemo, B. *Nanocatalysis. Nanoscience and Technology.*, chapter Lithographic Techniques in Nanocatalysis, pages 269–341. Springer, Berlin, Heidelberg, 2007. doi: 10.1007/978-3-540-32646-5.
- [11] Schauermann, S. and Freund, H.-J. Model Approach in Heterogeneous Catalysis: Kinetics and Thermodynamics of Surface Reactions. *Acc. Chem. Res.*, *48* (2015), 2775–2782. doi: 10.1021/acs.accounts.5b00237.
- [12] Papp, C. From Flat Surfaces to Nanoparticles: In Situ Studies of the Reactivity of Model Catalysts. *Catal. Lett.*, *147* (2017), 2–19. doi: 10.1007/s10562-016-1925-0.
- [13] Freund, H.-J. Model Systems in Heterogeneous Catalysis: Selectivity Studies at the Atomic Level. *Top. Catal.*, *48* (2008), 137–144. doi: 10.1007/s11244-008-9052-9.
- [14] Hansen, P. L.; Wagner, J. B.; Helveg, S.; Rostrup-Nielsen, J. R.; Clausen, B. S.; and Topsøe, H. Atom-Resolved Imaging of Dynamic Shape Changes in Supported Copper Nanocrystals. *Science*, *295* (2002), 2053–2055. doi: 10.1126/science.1069325.

- [15] Hävecker, M.; Wrabetz, S.; Kröhnert, J.; Csepei, L.-I.; Naumann d’Alnoncourt, R.; Kolen’ko, Y. V.; Girgsdies, F.; Schlögl, R.; and Trunschke, A. Surface Chemistry of Phase-Pure M1 MoVTaNb Oxide During Operation in Selective Oxidation of Propane to Acrylic Acid. *J. Catal.*, *285* (2012), 48–60. doi: 10.1016/j.jcat.2011.09.012.
- [16] Wettergren, K.; Hellman, A.; Cavalca, F.; Zhdanov, V. P.; and Langhammer, C. Unravelling the Dependence of Hydrogen Oxidation Kinetics on the Size of Pt Nanoparticles by in Operando Nanoplasmonic Temperature Sensing. *Nano Lett.*, *15* (2015), 574–580. doi: 10.1021/nl504042u.
- [17] Fritzsche, J.; Albinsson, D.; Fritzsche, M.; Antosiewicz, T. J.; Westerlund, F.; and Langhammer, C. Single Particle Nanoplasmonic Sensing in Individual Nanofluidic Channels. *Nano Lett.*, *16* (2016), 7857–7864. doi: 10.1021/acs.nanolett.6b04124.
- [18] Hoffmann, R. A Chemical and Theoretical Way to Look at Bonding on Surfaces. *Rev. Mod. Phys.*, *60* (1988), 601–628. doi: 10.1103/RevModPhys.60.601.
- [19] Hohenberg, P. and Kohn, W. Inhomogeneous Electron Gas. *Phys. Rev.*, *136* (1964), B864–B871. doi: 10.1103/PhysRev.136.B864.
- [20] Kohn, W. and Sham, L. J. Self-Consistent Equations Including Exchange and Correlation Effects. *Phys. Rev.*, *140* (1965), A1133–A1138. doi: 10.1103/PhysRev.140.A1133.
- [21] Nørskov, J. K.; Abild-Pedersen, F.; Studt, F.; and Bligaard, T. Density Functional Theory in Surface Chemistry and Catalysis. *PNAS*, *108* (2011), 937–943. doi: 10.1073/pnas.1006652108.
- [22] Van Santen, R. A. and Neurock, M. Concepts in Theoretical Heterogeneous Catalytic Reactivity. *Catal. Rev. Sci. Eng.*, *37* (1995), 557–698. doi: 10.1080/01614949508006451.
- [23] Kozlov, S. M. and Neyman, K. M. Insights from Methane Decomposition on Nanostructured Palladium. *J. Catal.*, *337* (2016), 111–121. doi: 10.1016/j.jcat.2016.02.010.
- [24] Fajín, J. L. C.; Bruix, A.; Cordeiro, M. N. D. S.; Gomes, J. R. B.; and Illas, F. Density Functional Theory Model Study of Size and Structure Effects on Water Dissociation by Platinum Nanoparticles. *J. Chem. Phys.*, *137* (2012), 034701. doi: 10.1063/1.4733984.
- [25] Jennings, P. C.; Aleksandrov, H. A.; Neyman, K. M.; and Johnston, R. L. A DFT study of Oxygen Dissociation on Platinum based Nanoparticles. *Nanoscale*, *6* (2014), 1153–1165. doi: 10.1039/c3nr04750d.
- [26] Viñes, F.; Lykhach, Y.; Staudt, T.; Lorenz, M. P. A.; Papp, C.; Steinrück, H.-P.; Libuda, J.; Neyman, K. M.; and Görling, A. Methane Activation by Platinum: Critical Role of Edge and Corner Sites of Metal Nanoparticles. *Chem. Eur. J.*, *16* (2010), 6530–6539. doi: 10.1002/chem.201000296.

- [27] Lopez-Acevedo, O.; Kacprzak, K. A.; Akola, J.; and Häkkinen, H. Quantum Size Effects in Ambient CO oxidation Catalysed by Ligand-Protected Gold Clusters. *Nat. Chem.*, *2* (2010), 329–334. doi: 10.1038/NCHEM.589.
- [28] Zheng, Z. and Greeley, J. Theoretical study of CO Adsorption on Au Catalysts under Environmental Catalytic Conditions. *Catal. Commun.*, *52* (2014), 78–83. doi: 10.1016/j.catcom.2014.03.016.
- [29] Yudanov, I. V.; Sahnoun, R.; Neyman, K. M.; Rösch, N.; Hoffmann, J.; Schauermaun, S.; Johánek, V.; Unterhalt, H.; Rupprechter, G.; Libuda, J.; and Freund, H.-J. CO Adsorption on Pd Nanoparticles: Density Functional and Vibrational Spectroscopy Studies. *J. Phys. Chem. B*, *107* (2003), 255–264. doi: 10.1021/jp022052b.
- [30] Posada-Borbón, A.; Heard, C. J.; and Grönbeck, H. Cluster Size Effects in Ethylene Hydrogenation over Palladium. *J. Phys. Chem. C*, *121* (2017), 10870–10875. doi: 10.1021/acs.jpcc.6b12072.
- [31] Kleis, J.; Greeley, J.; Romero, N. A.; Morozov, V. A.; Falsig, H.; Larsen, A. H.; Lu, J.; Mortensen, J. J.; Dulak, M.; Thygesen, K. S.; Nørskov, J. K.; and Jacobsen, K. W. Finite Size Effects in Chemical Bonding: From Small Clusters to Solids. *Catal. Lett.*, *141* (2011), 1067–1071. doi: 10.1007/s10562-011-0632-0.
- [32] Li, L.; Larsen, A. H.; Romero, N. A.; Morozov, V. A.; Glinsvad, C.; Abild-Pedersen, F.; Greeley, J.; Jacobsen, K. W.; and Nørskov, J. K. Investigation of Catalytic Finite-Size-Effects of Platinum Metal Clusters. *J. Phys. Chem. Lett.*, *4* (2013), 222–226. doi: 10.1021/jz3018286.
- [33] Newns, D. M. Self-Consistent Model of Hydrogen Chemisorption. *Phys. Rev.*, *178* (1969), 1123–1135. doi: 10.1103/PhysRev.178.1123.
- [34] Hammer, B. and Nørskov, J. K. Why Gold is the Noblest of All the Metals. *Nature*, *376* (1995), 238–240. doi: 10.1038/376238a0.
- [35] Stamatakis, M. Kinetic Modelling of Heterogeneous Catalytic Systems. *J. Phys.: Condens. Matter*, *27* (2015), 013001. doi: 10.1088/0953-8984/27/1/013001.
- [36] Prats, H.; Illas, F.; and Sayós, R. General Concepts, Assumptions, Drawbacks, and Misuses in Kinetic Monte Carlo and Microkinetic Modeling Simulations Applied to Computational Heterogeneous Catalysis. *Int. J. Quantum Chem.*, *118* (2017), e25518. doi: 10.1002/qua.25518.
- [37] Stoltze, P. and Nørskov, J. K. Bridging the "Pressure Gap" between Ultrahigh-Vacuum Surface Physics and High-Pressure Catalysis. *Phys. Rev. Lett.*, *55* (1985), 2502–2505. doi: 10.1103/PhysRevLett.55.2502.
- [38] Aparicio, L. M. and Dumesic, J. A. Ammonia Synthesis Kinetics: Surface Chemistry, Rate Expressions, and Kinetic Analysis. *Top. Catal.*, *1* (1994), 233–252. doi: 10.1007/BF01492278.

- [39] Aparicio, L. M.; Rossini, S. A.; Sanfilippo, D. G.; Rekoske, J. E.; Treviño, A. A.; and Dumesic, J. A. Microkinetic Analysis of Methane Dimerization Reaction. *Ind. Eng. Chem. Res.*, *30* (1991), 2114–2123. doi: 10.1021/ie00057a009.
- [40] Dahl, S.; Sehested, J.; Jacobsen, C. J. H.; Törnqvist, E.; and Chorkendorff, I. Surface Science Based Microkinetic Analysis of Ammonia Synthesis over Ruthenium Catalysts. *J. Catal.*, *192* (2000), 391–399. doi: 10.1006/jcat.2000.2857.
- [41] Dumesic, J. A. and Trevino, A. A. Kinetic Simulation of Ammonia Synthesis Catalysts. *J. Catal.*, *116* (1989), 119–129. doi: 10.1016/0021-9517(89)90080-8.
- [42] Frank, B.; Jentoft, F. C.; Soerijanto, H.; Kröhnert, J.; Schlögl, R.; and Schomäcker, R. Steam Reforming of Methanol over Copper-Containing Catalysts: Influence of Support Material on Microkinetics. *J. Catal.*, *246* (2007), 177–192. doi: 10.1016/j.jcat.2006.11.031.
- [43] Prasad, V.; Karim, A. M.; Arya, A.; and Vlachos, D. G. Assessment of Overall Rate Expressions and Multiscale, Microkinetic Model Uniqueness via Experimental Data Injection: Ammonia Decomposition on Ru/ γ -Al₂O₃ for Hydrogen Production. *Ind. Eng. Chem. Res.*, *48* (2009), 5255–5265. doi: 10.1021/ie900144x.
- [44] Stoltze, P. and Nørskov, J. K. An Interpretation of the High-Pressure Kinetics of Ammonia Synthesis Based on a Microscopic Model. *J. Catal.*, *110* (1988), 1–10. doi: 10.1016/0021-9517(88)90291-6.
- [45] Falsig, H.; Hvolbæk, B.; Kristensen, I. S.; Jiang, T.; Bligaard, T.; Christensen, C. H.; and Nørskov, J. K. Trends in the Catalytic CO Oxidation Activity of Nanoparticles. *Angew. Chem. Int. Ed.*, *47* (2008), 4835–4839. doi: 10.1002/anie.200801479.
- [46] Honkala, K.; Hellman, A.; Remediakis, I. N.; Logadottir, A.; Carlsson, A.; Dahl, S.; Christensen, C. H.; and Nørskov, J. K. Ammonia Synthesis from First-Principles Calculations. *Science*, *307* (2005), 555–558. doi: 10.1126/science.1106435.
- [47] Hansgen, D. A.; Vlachos, D. G.; and Chen, J. G. Using First Principles to Predict Bimetallic Catalysts for the Ammonia Decomposition Reaction. *Nat. Chem.*, *2* (2010), 484–489. doi: 10.1038/nchem.626.
- [48] Gokhale, A. A.; Dumesic, J. A.; and Mavrikakis, M. On the Mechanism of Low-Temperature Water Gas Shift Reaction on Copper. *J. Am. Chem. Soc.*, *130* (2008), 1402–1414. doi: 10.1021/ja0768237.
- [49] Van den Bossche, M. and Grönbeck, H. Methane Oxidation over PdO(101) Revealed by First-Principles Kinetic Modeling. *J. Am. Chem. Soc.*, *137* (2015), 12035–12044. doi: 10.1021/jacs.5b06069.
- [50] Trincherro, A.; Hellman, A.; and Grönbeck, H. Methane Oxidation over Pd and Pt studied by DFT and Kinetic Modeling. *Surf. Sci.*, *616* (2013), 206–213. doi: 10.1016/j.susc.2013.06.014.

- [51] Heard, C. J.; Hu, C.; Skoglundh, M.; Creaser, D.; and Grönbeck, H. Kinetic Regimes in Ethylene Hydrogenation over Transition-Metal Surfaces. *ACS Catal.*, *6* (2015), 3277–3286. doi: 10.1021/acscatal.5b02708.
- [52] Mei, D.; Du, J.; and Neurock, M. First-Principles-Based Kinetic Monte Carlo Simulation of Nitric Oxide Reduction over Platinum Nanoparticles under Lean-Burn Conditions. *Ind. Eng. Chem. Res.*, *49* (2010), 10364–10373. doi: 10.1021/ie100999e.
- [53] Loffreda, D.; Delbecq, F.; Vigné, F.; and Sautet, P. Catalytic Hydrogenation of Unsaturated Aldehydes on Pt(111): Understanding the Selectivity from First-Principles Calculations. *Angew. Chem. Int. Ed.*, *44* (2005), 5279–5282. doi: 10.1002/anie.200500913.
- [54] Yang, L.; Karim, A.; and Muckerman, J. T. Density Functional Kinetic Monte Carlo Simulation of Water-Gas Shift Reaction on Cu/ZnO. *J. Phys. Chem. C.*, *117* (2013), 3414–3425. doi: 10.1021/jp3114286.
- [55] Rogal, J.; Reuter, K.; and Scheffler, M. CO Oxidation on Pd(100) at Technologically Relevant Pressure Conditions: First-Principles Kinetic Monte Carlo study. *Phys. Rev. B*, *77* (2008), 155410. doi: 10.1103/PhysRevB.77.155410.
- [56] Piccinin, S. and Stamatakis, M. CO Oxidation on Pd(111): A First-Principles-Based Kinetic Monte Carlo Study. *ACS Catal.*, *4* (2014), 2143–2152. doi: 10.1021/cs500377j.
- [57] Kandoi, S.; Greeley, J.; Sanchez-Castillo, M. A.; Evans, S. T.; Gokhale, A. A.; Dumesic, J. A.; and Mavrikakis, M. Prediction of Experimental Methanol Decomposition Rates on Platinum from First Principles. *Top. Catal.*, *37* (2006), 17–28. doi: 10.1007/s11244-006-0001-1.
- [58] Zhdanov, V. P. and Kasemo, B. Monte Carlo Simulation of the Kinetics of Rapid Reactions on Nanometer Catalyst Particles. *Surf. Sci.*, *405* (1998), 27–37. doi: 10.1016/S0039-6028(97)01078-9.
- [59] Persson, H.; Thormählen, P.; Zhdanov, V. P.; and Kasemo, B. Monte Carlo Simulations of the Kinetics of Catalytic Reactions on Nanometer-Sized Particles, with Diffusion over Facet Boundaries. *J. Vac. Sci. Technol. A*, *17* (1999), 1721–1726. doi: 10.1116/1.581880.
- [60] Schlögl, R. Heterogeneous Catalysis. *Angew. Chem. Int. Ed.*, *54* (2015), 3465–3520. doi: 10.1002/anie.201410738.
- [61] Kohanoff, J. *Electronic Structure Calculations for Solids and Molecules: Theory and Computational Methods*. Cambridge University Press, New York (USA), 2006.
- [62] Perdew, J. P.; Burke, K.; and Ernzerhof, M. Generalized Gradient Approximation Made Simple. *Phys. Rev. Lett.*, *77* (1996), 3865–3868. doi: 10.1103/PhysRevLett.77.3865.

- [63] Hammer, B.; Hansen, L. B.; and Nørskov, J. K. Improved Adsorption Energetics within Density-Functional Theory using Revised Perdew-Burke-Ernzerhof Functionals. *Phys. Rev. B*, *59* (1999), 7413–7421. doi: 10.1103/PhysRevB.59.7413.
- [64] Haas, P.; Tran, F.; and Blaha, P. Calculation of the Lattice Constant of Solids with Semilocal Functionals. *Phys. Rev. B*, *79* (2009), 085104. doi: 10.1103/PhysRevB.79.085104.
- [65] Grimme, S.; Antony, J.; Ehrlich, S.; and Krieg, H. A Consistent and Accurate Ab Initio Parametrization of Density Functional Dispersion Correction (DFT-D) for the 94 Elements H-Pu. *J. Chem. Phys.*, *132* (2010), 154104. doi: 10.1063/1.3382344.
- [66] Blöchl, P. Projector Augmented-Wave Method. *Phys. Rev. B.*, *50* (1994), 17953–17979. doi: 10.1103/PhysRevB.50.17953.
- [67] Kittel, C. *Introduction to Solid State Physics*. John Wiley & Sons, Inc., Hoboken (USA), 8th edition edition, 2005.
- [68] Head, J. D. and Zerner, M. C. A Broyden–Fletcher–Goldfarb–Shanno Optimization Procedure for Molecular Geometries. *Chem. Phys. Lett.*, *122* (1985), 264–270. doi: 10.1016/0009-2614(85)80574-1.
- [69] Herring, C. Some Theorems on the Free Energies of Crystal Surfaces. *Phys. Rev.*, *82* (1951), 87–93. doi: 10.1103/PhysRev.82.87.
- [70] Baletto, F.; Ferrando, R.; Fortunelli, A.; Montalenti, F.; and Mottet, C. Crossover Among Structural Motifs in Transition and Noble-Metal Clusters. *J. Chem. Phys.*, *116* (2002), 3856. doi: 10.1063/1.1448484.
- [71] Mills, G.; Jónsson, H.; and Schenter, G. K. Reversible work Transition State Theory: Application to Dissociative Adsorption of Hydrogen. *Surf. Sci.*, *324* (1995), 305–337. doi: 10.1016/0039-6028(94)00731-4.
- [72] Henkelman, G.; Uberuaga, B. P.; and Jónsson, H. A Climbing Image Nudged Elastic Band Method for Finding Saddle Points and Minimum Energy Paths. *J. Chem. Phys.*, *113* (2000), 9901–9904. doi: 10.1063/1.1329672.
- [73] Hoffmann, M. J.; Medford, A. J.; and Bligaard, T. Framework for Scalable Adsorbate–Adsorbate Interaction Models. *J. Phys. Chem. C*, *120* (2016), 13087–13094. doi: 10.1021/acs.jpcc.6b03375.
- [74] Van den Bossche, M. and Grönbeck, H. Adsorbate Pairing on Oxide Surfaces: Influence on Reactivity and Dependence on Oxide, Adsorbate Pair, and Density Functional. *J. Phys. Chem. C*, *121* (2017), 8390–8398. doi: 10.1021/acs.jpcc.6b12789.
- [75] Jansen, A. P. J. *An Introduction to Kinetic Monte Carlo Simulations of Surface Reactions*. Springer, Berlin, Heidelberg, 2012. doi: 10.1007/978-3-642-29488-4.
- [76] Gould, H. and Tobochnik, J. *Statistical and Thermal Physics With Computer Applications*. Princeton University Press, Woodstock, Oxfordshire, 2010. P 318.

- [77] Campbell, C. T. and Sellers, J. R. V. The Entropies of Adsorbed Molecules. *J. Am. Chem. Soc.*, *134* (2012), 18109–18115. doi: 10.1021/ja3080117.
- [78] Sprowl, L. H.; Campbell, C. T.; and Árnadóttir, L. Hindered Translator and Hindered Rotor Models for Adsorbates: Partition Functions and Entropies. *J. Phys. Chem. C*, *120* (2016), 9719–9731. doi: 10.1021/acs.jpcc.5b11616.
- [79] Campbell, C. T.; Sprowl, L. H.; and Árnadóttir, L. Equilibrium Constants and Rate Constants for Adsorbates: Two-Dimensional (2D) Ideal Gas, 2D Ideal Lattice Gas, and Ideal Hindered Translator Models. *J. Phys. Chem. C*, *120* (2016), 10283–10297. doi: 10.1021/acs.jpcc.6b00975.
- [80] Qi, W.; Ran, J.; Wang, R.; Du, X.; Shi, J.; and Ran, M. Kinetic Mechanism of Effects of Hydrogen Addition on Methane Catalytic Combustion over Pt(111) Surface: A DFT Study with Cluster Modeling. *Comp. Mater. Sci.*, *111* (2016), 430–442. doi: 10.1016/j.commatsci.2015.09.002.
- [81] Hill, T. L. *Introduction to Statistical Thermodynamics*. Dover Publications Inc., New York, 1986. Chapter 9.
- [82] Bajpai, A.; Mehta, P.; Frey, K.; Lehmer, A. M.; and Schneider, W. F. Benchmark First-Principles Calculations of Adsorbate Free Energies. *ACS Catal.*, *8* (2018), 1945–1954. doi: 10.1021/acscatal.7b03438.
- [83] Piccini, G.; Alessio, M.; Sauer, J.; Zhi, Y.; Liu, Y.; Kolvenbach, R.; Jentys, A.; and Lercher, J. A. Accurate Adsorption Thermodynamics of Small Alkanes in Zeolites. Ab initio Theory and Experiment for H-Chabazite. *J. Phys. Chem. C*, *119* (2015), 6128–6137. doi: 10.1021/acs.jpcc.5b01739.
- [84] Paolucci, C.; Parekh, A. A.; Khurana, I.; Iorio, J. R. D.; Li, H.; Albarracín Caballero, J. D.; Shih, A. J.; Anggara, T.; Nicholas Delgass, W.; Miller, J. T.; Ribeiro, F. H.; Gounder, R.; and Schneider, W. F. Catalysis in a Cage: Condition-Dependent Speciation and Dynamics of Exchanged Cu Cations in SSZ-13 Zeolites. *J. Am. Chem. Soc.*, *138* (2016), 6028–6048. doi: 10.1021/jacs.6b02651.
- [85] Piccini, G. and Sauer, J. Effect of Anharmonicity on Adsorption Thermodynamics. *J. Chem. Theory Comput.*, *10* (2014), 2479–2487. doi: 10.1021/ct500291x.
- [86] Li, H.; Paolucci, C.; and Schneider, W. F. Zeolite Adsorption Free Energies from ab Initio Potentials of Mean Force. *J. Chem. Theory Comput.*, *14* (2018), 929–938. doi: 10.1021/acs.jctc.7b00716.
- [87] Nielsen, M.; Brogaard, R. Y.; Falsig, H.; Beato, P.; Swang, O.; and Svelle, S. Kinetics of Zeolite Dealumination: Insights from H-SSZ-13. *ACS Catal.*, *5* (2015), 7131–7139. doi: 10.1021/acscatal.5b01496.
- [88] Zhu, Y.-A.; Chen, D.; Zhou, X.-G.; and Yuan, W.-K. DFT Studies of Dry Reforming of Methane on Ni Catalyst. *Catal. Today.*, *148* (2009), 260–267. doi: 10.1016/j.cattod.2009.08.022.

- [89] Bligaard, T.; Nørskov, J. K.; Dahl, S.; Matthiesen, J.; Christensen, C. H.; and Sehested, J. The Brønsted–Evans–Polanyi Relation and the Volcano Curve in Heterogeneous Catalysis. *J. Catal.*, *224* (2004), 206–217. doi: 10.1016/j.jcat.2004.02.034.
- [90] Riedel, J. N.; Rötzer, M. D.; Jørgensen, M.; Vej-Hansen, U. G.; Pedersen, T.; Sebök, B.; Schweinberger, F. F.; Vesborg, P. C. K.; Hansen, O.; Schiøtz, J.; Heiz, U.; and Chorkendorff, I. H₂/D₂ Exchange Reaction on Mono-Disperse Pt Clusters: Enhanced Activity from Minute O₂ Concentrations. *Catal. Sci. Technol.*, *6* (2016), 6893–6900. doi: 10.1039/C6CY00756B.
- [91] Campbell, C. T.; Ertl, G.; Kuipers, H.; and Segner, J. A Molecular Beam Study of the Catalytic Oxidation of CO on a Pt(111) surface. *J. Chem. Phys.*, *73* (1980), 5862–5873. doi: 10.1063/1.440029.
- [92] Park, J. Y.; Zhang, Y.; Grass, M.; Zhang, T.; and Somorjai, G. A. Tuning of Catalytic CO Oxidation by Changing Composition of Rh-Pt Bimetallic Nanoparticles. *Nano Lett.*, *8* (2008), 673–677. doi: 10.1021/nl073195i.
- [93] Nakao, K.; Watanabe, O.; Sasaki, T.; Ito, S.-I.; Tomishige, K.; and Kunimori, K. CO Oxidation on Pd(111), Pt(111), and Rh(111) Surfaces studied by Infrared Chemiluminescence Spectroscopy. *Surf. Sci.*, *601* (2007), 3796–3800. doi: 10.1016/j.susc.2007.04.015.
- [94] Palmer, R. L. and Smith Jr., J. N. Molecular Beam Study of CO Oxidation on a (111) Platinum Surface. *J. Chem. Phys.*, *60* (1974), 1453–1463. doi: 10.1063/1.1681219.
- [95] Gerrard, A. L. and Weaver, J. F. Kinetics of CO Oxidation on High-Concentration Phases of Atomic Oxygen on Pt(111). *J. Chem. Phys.*, *123* (2005), 224703. doi: 10.1063/1.2126667.
- [96] Vogel, D.; Spiel, C.; Suchorski, Y.; Trincherro, A.; Schlögl, R.; and Rupprechter, G. Local Catalytic Ignition during CO Oxidation on Low-Index Pt and Pd Surfaces: A Combined PEEM, MS, and DFT Study. *Angew. Chem., Int. Ed.*, *51* (2012), 10041–10044. doi: 10.1002/anie.201204031.
- [97] Wrobel, R. J.; Becker, S.; and Weiss, H. Second/Additional Bistability in a CO Oxidation Reaction on Pt(111): An Extension and Compilation. *J. Phys. Chem. C*, *116* (2012), 22287–22292. doi: 10.1021/jp302270n.
- [98] Völkening, S. and Wintterlin, J. CO Oxidation on Pt(111) - Scanning Tunneling Microscopy Experiments and Monte Carlo Simulations. *J. Chem. Phys.*, *114* (2001), 6382–6395. doi: 10.1063/1.1343836.
- [99] Krick Calderón, S.; Grabau, M.; Óvári, L.; Kress, B.; Steinrück, H.-P.; and Papp, C. CO Oxidation on Pt(111) at Near Ambient Pressures. *J. Chem. Phys.*, *144* (2016), 044706. doi: 10.1063/1.4940318.
- [100] Alavi, A.; Hu, P.; Deutsch, T.; Silvestrelli, P. L.; and Hutter, J. CO Oxidation on Pt(111): An Ab Initio Density Functional Theory Study. *Phys. Rev. Lett.*, *80* (1998), 3650–3653. doi: 10.1103/PhysRevLett.80.3650.

- [101] Jones, E.; Oliphant, T.; Peterson, P.; and et al. SciPy: Open source scientific tools for Python, 2001. URL <https://docs.scipy.org/doc/scipy/reference/tutorial/integrate.html>, [Online; accessed 2017-05-10].
- [102] Iserles, A. *A First Course in the Numerical Analysis of Differential Equations*. Cambridge University Press, second edition edition, 2009. Chapter 2 - Multistep Methods.
- [103] Gillespie, D. T. A General Method for Numerically Simulating the Stochastic Time Evolution of Coupled Chemical Reactions. *J. Comput. Phys.*, *22* (1976), 403–434. doi: 10.1016/0021-9991(76)90041-3.
- [104] Chatterjee, A. and Vlachos, D. G. An Overview of Spatial Microscopic and Accelerated Kinetic Monte Carlo Methods. *J. Comput.-Aided Mater. Des.*, *14* (2007), 253–308. doi: 10.1007/s10820-006-9042-9.
- [105] Hoffmann, M. J.; Matera, S.; and Reuter, K. A Lattice Kinetic Monte Carlo Framework. *Comput. Phys. Commun.*, *185* (2014), 2138–2150. doi: 10.1016/j.cpc.2014.04.003.
- [106] Lukkien, J. J. Carlos. URL <https://carlos.win.tue.nl/>, [Online; accessed 2018-01-24].
- [107] Plimpton, S. S.; Thompson, A.; and Slepoy, A. SPPARKS Kinetic Monte Carlo Simulator. URL <http://spparks.sandia.gov/>, [Online; accessed 2018-01-24].
- [108] Leetmaa, M. and Skorodumova, N. V. KMCLib: A General Framework for Lattice Kinetic Monte Carlo (KMC) Simulations. *Comput. Phys. Commun.*, *185* (2014), 2340–2349. doi: 10.1016/j.cpc.2014.04.017.
- [109] Leetmaa, M. and Skorodumova, N. V. KMCLib 1.1: Extended Random Number Support and Technical Updates to the KMCLib General Framework for Kinetic Monte-Carlo Simulations. *Comput. Phys. Commun.*, *196* (2015), 611–613. doi: 10.1016/j.cpc.2015.06.016.
- [110] Kunz, L.; Kuhn, F. M.; and Deutschmann, O. Kinetic Monte Carlo Simulations of Surface Reactions on Supported Nanoparticles: A Novel Approach and Computer Code. *J. Chem. Phys.*, *143* (2015), 044108. doi: 10.1063/1.4926924.
- [111] Stamatakis, M. and Vlachos, D. G. A Graph-Theoretical Kinetic Monte Carlo Framework for On-Lattice Chemical Kinetics. *J. Chem. Phys.*, *134* (2011), 214115. doi: 10.1063/1.3596751.
- [112] Dybeck, E. C.; Plaisance, C. P.; and Neurock, M. Generalized Temporal Acceleration Scheme for Kinetic Monte Carlo Simulations of Surface Catalytic Processes by Scaling the Rates of Fast Reactions. *J. Chem. Theory Comput.*, *13* (2017), 1525–1538. doi: 10.1021/acs.jctc.6b00859.

- [113] Chatterjee, A. and Voter, A. F. Accurate Acceleration of Kinetic Monte Carlo Simulations through the Modification of Rate Constants. *J. Chem. Phys.*, *132* (2010), 194101. doi: 10.1063/1.3409606.
- [114] Fichthorn, K. A. and Lin, Y. A Local Superbasin Kinetic Monte Carlo Method. *J. Chem. Phys.*, *138* (2013), 164104. doi: 10.1063/1.4801869.
- [115] Puchala, B.; Falk, M. L.; and Garikipati, K. An Energy Basin Finding Algorithm for Kinetic Monte Carlo Acceleration. *J. Chem. Phys.*, *132* (2010), 134104. doi: 10.1063/1.3369627.
- [116] Zhu, G.; Han, J.; Zemlyanov, D. Y.; and Ribeiro, F. H. The Turnover Rate for the Catalytic Combustion of Methane over Palladium Is Not Sensitive to the Structure of the Catalyst. *J. Am. Chem. Soc.*, *126* (2004), 9896–9897. doi: 10.1021/ja049406s.
- [117] Zhu, G.; Han, J.; Zemlyanov, D. Y.; and Ribeiro, F. H. Temperature Dependence of the Kinetics for the Complete Oxidation of Methane on Palladium and Palladium Oxide. *J. Phys. Chem. B*, *109* (2005), 2331–2337. doi: 10.1021/jp0488665.
- [118] Monteiro, R.; Zemlyanov, D.; Storey, J. M.; and Ribeiro, F. H. Turnover Rate and Reaction Orders for the Complete Oxidation of Methane on a Palladium Foil in Excess Dioxygen. *J. Catal.*, *199* (2001), 291–301. doi: 10.1006/jcat.2001.3176.
- [119] Campbell, C. T. Future Directions and Industrial Perspectives Micro- and Macro-Kinetics: their Relationship in Heterogeneous Catalysis. *Top. Catal.*, *1* (1994), 353–366. doi: 10.1007/BF01492288.
- [120] Stegelmann, C.; Andreasen, A.; and Campbell, C. T. Degree of Rate Control: How Much the Energies of Intermediates and Transition States Control Rates. *J. Am. Chem. Soc.*, *131* (2009), 8077–8082. doi: 10.1021/ja9000097.
- [121] McNaught, A. D. and Wilkinson, D. *IUPAC. Compendium of Chemical Terminology*. Blackwell Scientific Publications, Oxford, 2nd ed. (the "gold book") edition, 1997. URL <https://doi.org/10.1351/goldbook.004322>, [Online; accessed 2019-02-19].
- [122] G  lin, P. and Primet, M. Complete Oxidation of Methane at Low Temperature over Noble Metal Based Catalysts: a Review. *Appl. Catal. B-Environ.*, *39* (2002), 1–37. doi: 10.1016/S0926-3373(02)00076-0.
- [123] Hoffund, G. B.; Li, Z.; Epling, W. S.; G  bel, T.; Schneider, P.; and Hahn, H. Catalytic Methane Oxidation Over Pd Supported on Nanocrystalline and Polycrystalline TiO₂ Mn₃O₄, CeO₂ and ZrO₂. *React. Kinet. Catal. Lett.*, *70* (2000), 97–103. doi: 10.1023/A:1010362632223.
- [124] Hao, H.; Liu, Z.; Zhao, F.; and Li, W. Natural Gas as Vehicle Fuel in China: A Review. *Renewable Sustainable Energy Rev.*, *62* (2016), 521–533. doi: 10.1016/j.rser.2016.05.015.

- [125] Burch, R.; Loader, P.; and Urbano, F. Some Aspects of Hydrocarbon Activation on Platinum Group Metal Combustion Catalysts. *Catal. Today*, *27* (1996), 243–248. doi: 10.1016/0920-5861(95)00194-8.
- [126] Farrauto, R. J.; Hobson, M. C.; Kennelly, T.; and Waterman, E. M. Catalytic Chemistry of Supported Palladium for Combustion of Methane. *Appl. Catal. A-Gen.*, *81* (1992), 227–237. doi: 10.1016/0926-860X(92)80095-T.
- [127] Lundgren, E.; Gustafson, J.; Mikkelsen, A.; Andersen, J. N.; Stierle, A.; Dosch, H.; Todorova, M.; Rogal, J.; Reuter, K.; and Scheffler, M. Kinetic Hindrance during the Initial Oxidation of Pd(100) at Ambient Pressures. *Phys. Rev. Lett.*, *92* (2004), 046101. doi: 10.1103/PhysRevLett.92.046101.
- [128] Ketteler, G.; Ogletree, D. F.; Bluhm, H.; Liu, H.; Hebenstreit, E. L. D.; and Salmeron, M. In Situ Spectroscopic Study of the Oxidation and Reduction of Pd(111). *J. Am. Chem. Soc.*, *127* (2005), 18269–18273. doi: 10.1021/ja055754y.
- [129] Baldwin, T. R. and Burch, R. Catalytic Combustion of Methane over Supported Palladium Catalysts: II. Support and Possible Morphological Effects. *Appl. Catal.*, *66* (1990), 359–381. doi: 10.1016/S0166-9834(00)81649-8.
- [130] Hicks, R. F.; Qi, H.; Young, M. L.; and Lee, R. G. Structure Sensitivity of Methane Oxidation over Platinum and Palladium. *J. Catal.*, *122* (1990), 280–294. doi: 10.1016/0021-9517(90)90282-O.
- [131] Hicks, R. F.; Qi, H.; Young, M. L.; and Lee, R. G. Effect of Catalyst Structure on Methane Oxidation over Palladium on Alumina. *J. Catal.*, *122* (1990), 295–306. doi: 10.1016/0021-9517(90)90283-P.
- [132] Oh, S. H.; Mitchell, P. J.; and Siewert, R. M. Methane Oxidation over Alumina-Supported Noble Metal Catalysts With and Without Cerium Additives. *J. Catal.*, *132* (1991), 287–301. doi: 10.1016/0021-9517(91)90149-X.
- [133] Ciuparu, D.; Lyubovsky, M. R.; Altman, E.; Pfefferle, L. D.; and Datye, A. Catalytic Combustion of Methane over Palladium-based Catalysts. *Cat. Rev. - Sci. Eng.*, *44* (2002), 593–649. doi: 10.1081/CR-120015482.
- [134] van Spronsen, M. A.; Frenken, J. W. M.; and Groot, I. M. N. Surface Science under Reaction Conditions: CO Oxidation on Pt and Pd Model Catalysts. *Chem. Soc. Rev.*, *46* (2017), 4347–4374. doi: 10.1039/C7CS00045F.
- [135] Kyriakou, G.; Boucher, M. B.; Jewell, A. D.; Lewis, E. A.; Lawton, T. J.; Baber, A. E.; Tierney, H. L.; Flytzani-Stephanopoulos, M.; and Sykes, E. C. H. Isolated Metal Atom Geometries as a Strategy for Selective Heterogeneous Hydrogenations. *Science*, *335* (2012), 1209–1212. doi: 10.1126/science.1215864.
- [136] Boucher, M. B. Single Atom Alloy Surface Analogs in Pd_{0.18}Cu₁₅ Nanoparticles for Selective Hydrogenation Reactions. *Phys. Chem. Chem. Phys.*, *15* (2013), 12187–12196. doi: 10.1039/c3cp51538a.

- [137] Cheng, Z.; Fine, N. A.; and Lo, C. S. Platinum Nanoclusters Exhibit Enhanced Catalytic Activity for Methane Dehydrogenation. *Top. Catal.*, *55* (2012), 345–352. doi: 10.1007/s11244-012-9803-5.
- [138] Jiang, T.; Mowbray, D. J.; Dobrin, S.; Falsig, H.; Hvolbæk, B.; Bligaard, T.; and Nørskov, J. K. Trends in CO Oxidation Rates for Metal Nanoparticles and Close-Packed, Stepped, and Kinked Surfaces. *J. Phys. Chem. C*, *113* (2009), 10548–10553. doi: 10.1021/jp811185g.
- [139] Hvolbæk, B.; Janssens, T. V. W.; Clausen, B. S.; Falsig, H.; Christensen, C. H.; and Nørskov, J. K. Catalytic Activity of Au Nanoparticles. *Nano Today*, *2* (2007), 14–18. doi: 10.1016/S1748-0132(07)70113-5.
- [140] Brodersen, S. H.; Grønbjerg, U.; Hvolbæk, B.; and Schiøtz, J. Understanding the Catalytic Activity of Gold Nanoparticles through Multi-Scale Simulations. *J. Catal.*, *284* (2011), 34–41. doi: 10.1016/j.jcat.2011.08.016.
- [141] Calle-Vallejo, F.; Martínez, J. I.; García-Lastra, J. M.; Sautet, P.; and Loffreda, D. Fast Prediction of Adsorption Properties for Platinum Nanocatalysts with Generalized Coordination Numbers. *Angew. Chem., Int. Ed.*, *53* (2014), 8316–8319. doi: 10.1002/anie.201402958.
- [142] Calle-Vallejo, F.; Loffreda, D.; Koper, M. T. M.; and Sautet, P. Introducing Structural Sensitivity into Adsorption–Energy Scaling Relations by means of Coordination Numbers. *Nat. Chem.*, *7* (2015), 403–410. doi: 10.1038/nchem.2226.
- [143] Calle-Vallejo, F.; Tymoczko, J.; Colic, V.; Vu, Q. H.; Pohl, M. D.; Morgenstern, K.; Loffreda, D.; Sautet, P.; Schuhmann, W.; and Bandarenka, A. S. Finding Optimal Surface Sites on Heterogeneous Catalysts by Counting Nearest Neighbors. *Science*, *350* (2015), 185–189. doi: 10.1126/science.aab3501.
- [144] Roling, L. T. and Abild-Pedersen, F. Structure-Sensitive Scaling Relations: Adsorption Energies from Surface Site Stability. *ChemCatChem*, *10* (2018), 1643–1650. doi: 10.1002/cctc.201701841.
- [145] Kozuch, S. Steady State Kinetics of Any Catalytic Network: Graph Theory, the Energy Span Model, the Analogy between Catalysis and Electrical Circuits, and the Meaning of “Mechanism”. *ACS Catal.*, *5* (2015), 5242–5255. doi: 10.1021/acscatal.5b00694.
- [146] Pingel, T. N.; Fouladvand, S.; Heggen, M.; Dunin-Borkowski, R. E.; Jäger, W.; Westenberger, P.; Phifer, D.; McNeil, J.; Skoglundh, M.; Grönbeck, H.; and Olsson, E. Three-Dimensional Probing of Catalyst Ageing on Different Length Scales: A Case Study of Changes in Microstructure and Activity for CO oxidation of a Pt-Pd/Al₂O₃ Catalyst. *ChemCatChem*, *9* (2017), 3544–3553. doi: 10.1002/cctc.201700479.
- [147] Yarulin, A. E.; Crespo-Quesada, R. M.; Egorova, E. V.; and Kiwi-Minsker, L. L. Structure Sensitivity of Selective Acetylene Hydrogenation over the Catalysts with Shape Controlled Palladium Nanoparticles. *Kinet. Catal.*, *53* (2012), 253–261. doi: 10.1134/S0023158412020152.

- [148] Grabow, L.; Xu, Y.; and Mavrikakis, M. Lattice Strain Effects on CO Oxidation on Pt(111). *Phys. Chem. Chem. Phys.*, *8* (2006), 3369–3374. doi: 10.1039/b606131a.
- [149] Li, L.; Abild-Pedersen, F.; Greeley, J.; and Nørskov, J. K. Surface Tension Effects on the Reactivity of Metal Nanoparticles. *J. Phys. Chem. Lett.*, *6* (2015), 3797–3801. doi: 10.1021/acs.jpcclett.5b01746.
- [150] Francis, M. F. and Curtin, W. A. Mechanical Stress Combined with Alloying May Allow Continuous Control Over Reactivity: Strain Effects on CO Dissociation and Subsequent Methanation Catalysis over Ni(211), Ni₃Fe(211), and NiFe(112). *J. Phys. Chem. C*, *121* (2017), 6113–6119. doi: 10.1021/acs.jpcc.6b12329.
- [151] Greeley, J. and Mavrikakis, M. Methanol Decomposition on Cu(111): A DFT Study. *J. Catal.*, *208* (2002), 291–300. doi: 10.1006/jcat.2002.3586.
- [152] Michalak, W. D.; Krier, J. M.; Komvopoulos, K.; and Somorjai, G. A. Structure Sensitivity in Pt Nanoparticle Catalysts for Hydrogenation of 1,3-Butadiene: In Situ Study of Reaction Intermediates Using SFG Vibrational Spectroscopy. *J. Phys. Chem. C*, *117* (2013), 1809–1817. doi: 10.1021/jp311772p.
- [153] Wang, R.; He, H.; Wang, J.; Liu, L.; and Dai, H. Shape-Regulation: An Effective Way to Control CO Oxidation Activity over Noble Metal Catalysts. *Catal. Today*, *201* (2013), 68–78. doi: 10.1016/j.cattod.2012.03.082.
- [154] Shandiz, M. A.; Safaei, A.; Sanjabi, S.; and Barber, Z. H. Modeling the Cohesive Energy and Melting Point of Nanoparticles by their Average Coordination Number. *Solid State Commun.*, *145* (2008), 432–437. doi: 10.1016/j.ssc.2007.12.021.
- [155] Holman, S. W. and Lawrence, L., R. R. and Barr. Melting Points of Aluminum, Silver, Gold, Copper, and Platinum. *Proc. Am. Acad. Arts Sci.*, *31* (1985), 218–233. doi: 10.2307/20020628.
- [156] Mavrikakis, M.; Hammer, B.; and Nørskov, J. K. Effect of Strain on the Reactivity of Metal Surfaces. *Phys. Rev. Lett.*, *81* (1998), 2819–2822. doi: 10.1103/PhysRevLett.81.2819.
- [157] Nielsen, J.; d’Avezac, M.; Hetherington, J.; and Stamatakis, M. Parallel Kinetic Monte Carlo Simulation Framework Incorporating Accurate Models of Adsorbate Lateral Interactions. *J. Chem. Phys.*, *139* (2013), 224706. doi: 10.1063/1.4840395.